

SENSITIVITY OF TURBULENCE CLOSURE COEFFICIENTS ON THE  
AERODYNAMIC PREDICTIONS OF FLOW OVER A SIMPLIFIED ROAD  
VEHICLE

by

Chamundeswar Sridhar Dangeti

A thesis submitted to the faculty of  
The University of North Carolina at Charlotte  
in partial fulfillment of the requirements  
for the degree of Master of Science in  
Mechanical Engineering

Charlotte

2018

Approved by:

---

Dr. Mesbah Uddin

---

Dr. Peter T. Tkacik

---

Dr. Christopher Vermillion

©2018  
Chamundeswar Sridhar Dangeti  
ALL RIGHTS RESERVED

## ABSTRACT

CHAMUNDESWAR SRIDHAR DANGETI. Sensitivity of turbulence closure coefficients on the aerodynamic predictions of flow over a simplified road vehicle. (Under the direction of DR. MESBAH UDDIN)

Computational Fluid Dynamics (CFD) analysis of complex external flows is an important component of road vehicle design and development. The Reynolds Averaged Navier Stokes (RANS) turbulence modeling is widely used in the automotive industry for simulating these complex flows, because of its short turnover time and cost-effectiveness. Existing literature shows that the popular two-equation turbulence models like, the SST  $k - \omega$  turbulence model, fail to produce good flow predictions when applied to a simplified car geometry, such as the Ahmed body, which exhibits flow features similar to real automotive flows. The present study improves the prediction capabilities of the SST  $k - \omega$  turbulence model by tuning a few selected turbulence model closure coefficients for the  $25^\circ$  rear slant angle ( $\phi = 25^\circ$ ) Ahmed body. This involves studying individual effects of these closure coefficients and then formulating a combination of these parameters that yields the best correlation with the experimental data. The best combination thus attained is then applied to scale resolved simulations such as the Improved Delayed Detached Eddy simulations (IDDES) for improved flow predictions. The tuning of closure coefficients was further applied to Ahmed body geometry with different slant angles ( $\phi = 20^\circ$  and  $\phi = 35^\circ$ ). The present study reveals that a combination of the closure coefficients can be obtained that can lead to very well correlated force and flow predictions for each of the Ahmed body configurations. However, this tuned combination is not universal, and each slant angle requires a different combination of model closure coefficients. This, in turn, questions the validity of equilibrium assumptions used in postulating the turbulence model transport equations for flows with massive separation and reattachment.

## ACKNOWLEDGEMENTS

First, I would like to express my gratitude by thanking my advisor, Dr. Mesbah Uddin, without whom I would not be able to accomplish the work presented in this thesis. It was he who foresaw my capabilities and accepted me to work with him. During the course of our journey, his thoughtful insights into my way of thinking and approach have helped me to develop and transform into a professional engineer. Second, I would like to thank Dr. Peter T. Tkacik and Dr. Christopher Vermillion for taking their time to review my thesis and provided their perceptions to refine the thesis. I am thankful to the colleagues of my research group, specially Chunhui Zhang, Chen Fu, Sudhan Rajashekar and Adit Misar who helped me at times where I struggled. Last but not least, I would like to thank the Mechanical Engineering Department and UNC Charlotte High-Performance Computing Group for supporting my research, especially Jon Halter, who responded quickly and helped in solving the job issues on the cluster.

## DEDICATION

To my parents, girlfriend and friends for all their support that they have given throughout this process.

## TABLE OF CONTENTS

LIST OF FIGURES	viii
LIST OF TABLES	xi
LIST OF SYMBOLS	1
CHAPTER 1: INTRODUCTION	1
1.1. Motivation	2
1.2. Objectives of Study	3
1.3. Organization of Thesis	3
CHAPTER 2: Literature Review	4
2.1. CFD investigations on Ahmed body	8
CHAPTER 3: Turbulence Modeling	12
3.1. Turbulence Modeling	13
3.2. Classification of Turbulence Models	14
3.2.1. Direct Numerical Simulation (DNS)	14
3.2.2. Large Eddy Simulation (LES)	15
3.2.3. Detached Eddy Simulation (DES)	15
3.2.4. Reynolds Averaged Navier Stokes (RANS)	16
3.3. Choice of Turbulence model for the study	16
CHAPTER 4: NUMERICAL SETUP	20
4.1. Ahmed body model	20
4.2. Mesh Setup	21
4.3. Boundary conditions	26

	vii
4.4. Physics Setup	27
CHAPTER 5: Results and Discussions	30
5.1. Mesh Independence Study	30
5.2. Effect of closure coefficients on the force predictions	31
5.3. Effect of closure coefficients on the flow predictions	36
5.4. Validation of the tuned set of closure coefficients	48
5.5. Implementation of closure coefficients modification for other rear slant angles	63
CHAPTER 6: CONCLUSIONS	66
6.1. Future Research	68
REFERENCES	69

## LIST OF FIGURES

FIGURE 2.1: CFD of a generic road vehicle.	4
FIGURE 2.2: Flow features over a Ahmed body.	5
FIGURE 2.3: Experimental setup of Strachan.	8
FIGURE 2.4: Instantaneous flow field for LES of Ahmed body.	9
FIGURE 2.5: Instantaneous Iso-surfaces of pressure in the far wake.	10
FIGURE 3.1: Turbulence Energy Spectrum.	14
FIGURE 4.1: Schematic diagram of Ahmed body used in this thesis.	20
FIGURE 4.2: Mesh scene with overhead sting at the center plane $Y=0$ .	23
FIGURE 4.3: Mesh scene without overhead sting at the center plane $Y=0$ .	24
FIGURE 4.4: Mesh scene near the slant.	24
FIGURE 4.5: Mesh scene with overhead sting at the center plane $X=0$ .	25
FIGURE 4.6: Mesh scene without overhead sting at the center plane $X=0$ .	25
FIGURE 4.7: Mesh scene at the center plane $Z=0$ .	26
FIGURE 4.8: Computational Domain with boundary conditions.	27
FIGURE 5.1: Comparison of Baseline SST Model against CFD work done in Literature.	32
FIGURE 5.2: Percentage relative deviation of $C_d$ and $C_l$ from modification of coefficients against the experiment.	35
FIGURE 5.3: Contours of Skin friction coefficient over the rear slant for different values of $\sigma_{\omega 2}$	37
FIGURE 5.4: Contours of Normalized TKE over the rear slant for different values of $\sigma_{\omega 2}$ .	38
FIGURE 5.5: Contours of Normalized Vorticity (i) over the rear slant for different values of $\sigma_{\omega 2}$ .	39

FIGURE 5.6: Contours of Streamlines in the wake for different values of $\sigma_{\omega 2}$ .	40
FIGURE 5.7: Contours of Skin friction coefficient over the slant for different values of $\sigma_{\omega 1}$ .	42
FIGURE 5.8: Contours of Normalized TKE over the slant for different values of $\sigma_{\omega 1}$ .	43
FIGURE 5.9: Contours of Normalized vorticity (i) over the slant for different values of $\sigma_{\omega 1}$ .	44
FIGURE 5.10: Contours of Skin friction coefficient over the slant for combination of $\sigma_{\omega 1}$ and $\sigma_{\omega 2}$ .	45
FIGURE 5.11: Contours of Skin friction coefficient over the slant for combination of $\sigma_{\omega 1}$ and $\sigma_{\omega 2}$ .	45
FIGURE 5.12: Contours of Streamlines for different combination of $\sigma_{\omega 1}$ and $\sigma_{\omega 2}$ and $\beta^*$ .	47
FIGURE 5.13: Streamwise velocity profiles over the slant	50
FIGURE 5.14: Transverse velocity profiles of normalized stream wise velocity over the trailing edge of the Ahmed body	51
FIGURE 5.15: Transverse velocity profiles of normalized Stream wise velocity comparison	52
FIGURE 5.16: Transverse velocity profiles of normalized vertical velocity over the trailing edge of the Ahmed body	53
FIGURE 5.17: Transverse velocity profiles of normalized vertical velocity comparison	54
FIGURE 5.18: Transverse velocity profiles of normalized stream wise velocity at location $x/L = 0.5$ and $y/L = 0.15$	55
FIGURE 5.19: Transverse velocity profiles of normalized vertical velocity at location $x/L = 0.5$ and $y/L = 0.15$	56
FIGURE 5.20: Contour plots of normalized streamwise velocity at location $x/L = 0.077$	57

FIGURE 5.21: Contour plots of normalized streamwise velocity at location $x/L=0.5$	58
FIGURE 5.22: Contour plots of normalized streamwise velocity at location $x/L=1$	59
FIGURE 5.23: Contour plots of coefficient of pressure distribution over the rear slant	61
FIGURE 5.24: Streamlines in the wake of the Ahmed body	62
FIGURE 5.25: Iso surfaces of Normalized Q-criterion = 60.	63

## LIST OF TABLES

TABLE 4.1: Example of short label.	26
TABLE 4.2: Boundary conditions.	27
TABLE 4.3: Physics setup for Steady RANS Simulations.	28
TABLE 4.4: Physics setup for IDDES Simulations.	29
TABLE 5.1: Comparison between half body and Full body simulations.	30
TABLE 5.2: Mesh Independence Study.	31
TABLE 5.3: Comparison of $C_d$ and $C_l$ for Baseline case	31
TABLE 5.4: Comparison of $C_d$ and $C_l$ for different values of $\sigma_{\omega 1}$	34
TABLE 5.5: Comparison of $C_d$ and $C_l$ for different values of $\sigma_{\omega 2}$	34
TABLE 5.6: Comparison of $C_d$ and $C_l$ for different values of $\beta^*$	34
TABLE 5.7: Comparison of $C_d$ and $C_l$ for different combinations of $\sigma_{\omega 1}$ , $\sigma_{\omega 2}$ and $\beta^*$	46
TABLE 5.8: Comparison of $C_d$ and $C_l$ for With and without support sting	48
TABLE 5.9: Comparison of $C_d$ and $C_l$ for With and without support sting	49
TABLE 5.10: Comparison of $C_d$ and $C_l$ for Ahmed body with rear slant angle $\phi=20^\circ$	64
TABLE 5.11: Comparison of $C_d$ and $C_l$ for Ahmed body with rear slant angle $\phi=35^\circ$	65
TABLE 5.12: Best results for Ahmed body with all rear slant angles.	65

## CHAPTER 1: INTRODUCTION

Computational Fluid Dynamics (CFD) has evolved into a powerful tool in many industries by providing solutions for complex flow problems. Technological advancements in computer hardware and software boosted the accuracy of the CFD techniques and made them an ideal tool to design and develop new complex products quicker and cheaper. The ability to solve problems involving fluid flow numerically reduces the dependence on physical testing. In spite of being a powerful tool, CFD has its own limitations.

The Navier-Stokes equations govern the motion of fluids. There is no analytical solution to these equations, which puts in the need for numerical methods for solving them. The discretization process may be straightforward for simple problems, but the required spatial and temporal resolution to resolve the turbulent scales demand high computational power and time. Turbulence modeling reduces the need to resolve the computational domain at Kolmogorov scales representing the smallest scale in a turbulent flow, but, on the other hand, these models cannot accurately predict the fluid flow or body forces for all possible flow configurations. The available turbulence models require intimate knowledge of their functionality and limitations in order to implement correctly within the CFD simulations and to provide accurate flow predictions.

An industry where CFD is gaining importance as a predictive tool is the automotive industry, where testing and development of new vehicles is costly and time-consuming. CFD provides additional testing capabilities in the field where design optimization is of paramount importance. Automotive industries are consistently leaning towards CFD as a preparatory design tool for more in-depth analysis of the flow field that

wind tunnel testing is unable to provide.

The desire to improve fuel efficiency for the passenger vehicles and performance of the race cars, reliable CFD simulations of complex separated turbulent flows around the vehicles has become a crucial goal. Due to the complex car geometries, validation of high-order turbulence simulations is computationally expensive and often are case specific. Flow around simplified geometries, that reproduces the basic aerodynamic features observed in real automotive flows has gained importance in the automotive industry. These simplified geometries were used for validating the turbulence modeling approaches by comparing numerical results with the experimental data.

## 1.1 Motivation

The Ahmed car body[1] represents a generic car geometry with a slanted back and has been tested extensively in the literature. In spite of being a simplified model of the real car, it is a challenging test case for turbulence modeling community as it provides many of the flow features present in reality such as separation and reattachment behind the body and complex vortex interactions, that occur in the wake. The strength of separation mainly depends on the slant angle in a complex manner. Experimentally it has been observed that at the slant angle of  $30^\circ$  the flow completely separates over the entire slant back of the body, because of the weaker counter-rotating vortices and at a slant angle of  $25^\circ$ , the flow separates and reattaches on the rear slant of the body, because of the presence of stronger counter-rotating vortices. Majority of the RANS models were able to predict separation, but failed to predict reattachment on the slant for  $25^\circ$  rear slant angle. This phenomenon is the primary objective of this work which aims at investigating the behavior of the standard k-omega SST RANS model and then fine-tuning the turbulence model closure coefficients for better force and flow predictions.

## 1.2 Objectives of Study

This thesis investigates the veracity of SST  $k-\omega$  turbulence model in predicting the flow over an Ahmed body with  $25^\circ$  rear slant angle. From the literature, it is known that the default SST  $k-\omega$  turbulence model fails to predict the actual flow. This thesis is driven to improve the performance SST  $k-\omega$  turbulence model, by modifying the turbulent closure coefficients for better force and flow predictions. Formulation of the best combination of closure coefficients for the  $25^\circ$  rear slant angle, based on the closure coefficient sensitivity analysis. Application of the best combination of closure coefficients to scale resolved simulations such as Improved Delayed Detached Eddy Simulations (IDDES) for improved flow predictions. Formulating best combination of closure coefficients for Ahmed body with different slant angles ( $\phi = 20^\circ$  and  $35^\circ$ ).

## 1.3 Organization of Thesis

Chapter 1 indicated the motivations for the thesis and provided a basic structure that the thesis will follow.

Chapter 2 gives a brief literature review of experimental and computational studies of Ahmed body.

Chapter 3 provides a brief understanding of turbulence modeling and the turbulence models used in this thesis.

Chapter 4 provides information on meshing strategies used for meshing the model, Simulation setup, and Boundary conditions.

Chapter 5 contains results discussion of various simulations. These include mesh independence study, effects of turbulence closure coefficients, formulating the best set of closure parameters for the chosen turbulence model and its validation.

Chapter 6 concludes all sections and provides the scope of future work in this study.

## CHAPTER 2: Literature Review

CFD analysis of road vehicles is a complex problem as it involves resolving and predicting intricate flow features which include massive flow separation, reattachment, and flow interactions, see Figure 2.1. In order to model a road vehicle, we need to take into account the rotating wheels, underbody components and small components that affect the flow field such as side mirrors. Simulating these models which represent the actual geometry requires very high computational time and power. Due to these challenges modeling a simplified road vehicle, that can replicate all the intricate flow features came into limelight. Even though these were simplified versions of the realistic models, they exhibit flow features which are observed in a real automotive model.

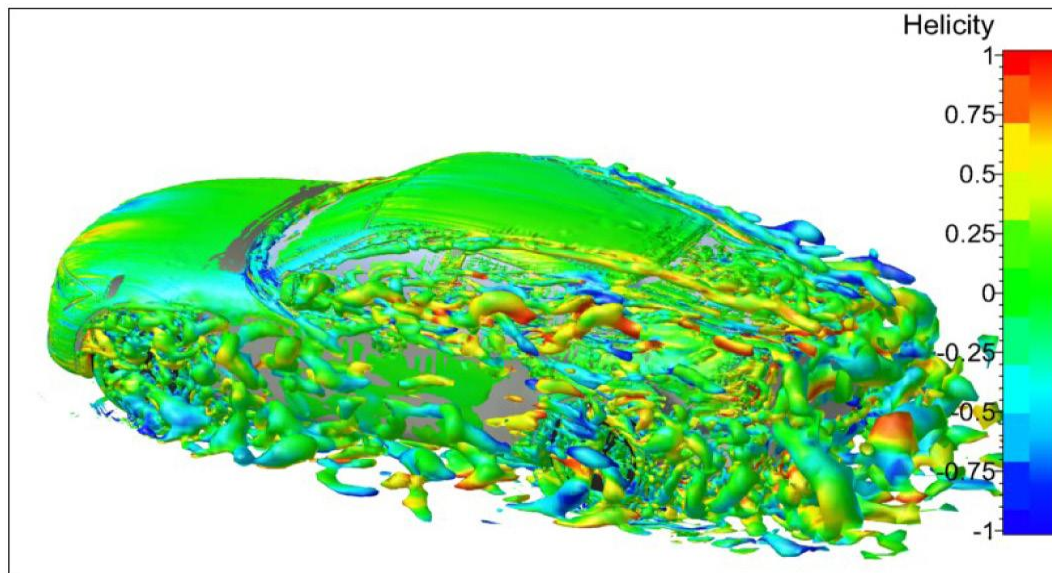


Figure 2.1: CFD of a generic road vehicle showing complex flow features[2].

Among the generic car models, DrivAer model[3] is popular, as its geometry is more realistic with all the essential components of an automobile. The experimental data

was made available to researchers for validating their CFD findings. Advancement in computational technology boosted the studies of complex flows around these realistic bodies. Even though these new simulations predicting the trends similar to the experimental data, the intricate flows and interactions were not reproduced accurately in CFD, because of its inability to model the entire band of turbulent scales.

A Simple model can be used to resolve these flows with the focus on the fundamental characteristics of the flow. One such model is the Ahmed model introduced by Ahmed et al.[1] which has flow characteristics similar to a regular automotive vehicle. The Ahmed model is a parallelepiped having round edges with the orientation towards the direction of the flow with a slanted face at the rear.

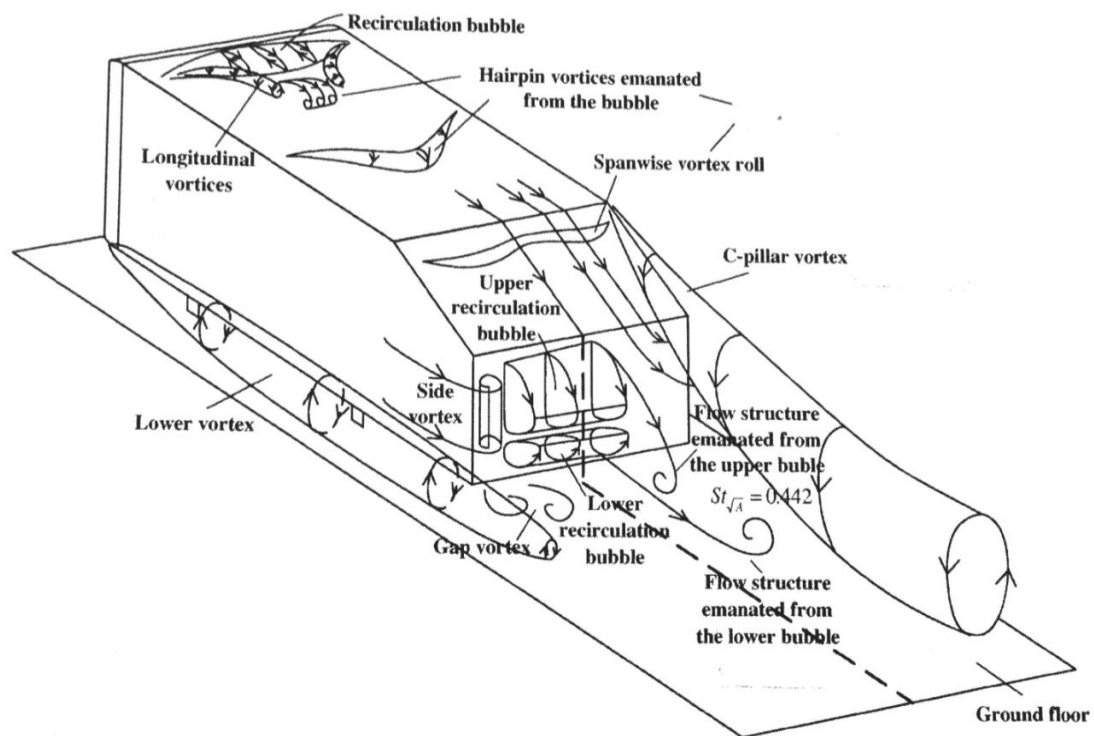


Figure 2.2: Detailed Flow features over a Ahmed body[4].

The flow characteristics of the Ahmed body is governed by the rear slant angle ( $\phi$ ), that affects the wake behavior. Recirculation behind the body, flow separation from the rear slant, counter rotating vortices generated by the rear slant are the major flow

characteristics that affect the modern vehicles and can be observed in this model. A detailed idea about the complexity of the problem can be understood from Figure 2.2. The flow separation and interaction of the vortices are the complexities that the turbulence models fail to predict in CFD.

The abundance availability of the experimental data on the Ahmed body and the simplicity of the model, made it an ideal subject for this study. The CAD model was created using Solidworks software and is used in the subsequent simulations. Since the Ahmed model is a simplified geometry the amount of computational power required will be less than the actual car geometry. These advantages led to inclusion of the Ahmed model in this thesis.

Originally the experiments on Ahmed body were conducted by Ahmed.et.al[1] with stilts in a wind tunnel having a stationary ground with a Reynolds number based on vehicle length of 1044 *mm* is  $4.29 \times 10^6$ . The slant angle is varied from 0 to 40 degrees. From this experiment, it was found that 85 percent of the drag was attributed to the pressure drag and therefore the pressure recovery resulted in lower drag coefficients. It was observed that the critical angle occurs at 30 degrees, where the drag coefficient reached a maximum of 0.378 (high drag configuration) before the flow separates from the slant and the drag coefficient drops to 0.260 (low drag coefficient). The high drag configuration is the original body, whereas the low configuration has a splitter plate vertically on the symmetry plane[1]. The original experiment did not report lift coefficients, whereas other experiments based on similar setup reported lift coefficients for the better understanding of the flow characteristics.

Several follow up studies have been performed in CFD and within the wind tunnel after the original experiment has been carried out. Majority of these experiments focused on the critical angle ( $\phi=30^\circ$ ), subcritical angle ( $\phi=25^\circ$ ) and supercritical angle ( $\phi=35^\circ$ ). These angles can produce flows that can be, separate and re-attach on the rear slant at the subcritical angle, tripped into high or low drag configurations at the

critical angle and separated flow on the rear slant angle at the super-critical angle. The change in the rear slant angle produces an adverse pressure gradient at the beginning of the rear slant, due to which the turbulent kinetic energy gets energized and results in a complex flow.

A few prominent studies that are well acclaimed and accepted from the literature will be discussed. Lienhart[5] in his experiment performed a Laser Doppler Anemometry(LDA), Particle Image Velocimetry (PIV), and Hotwire Anemometer measurements of the Ahmed body in a stationary wind tunnel for subcritical and supercritical angles at free stream velocity of  $40\text{ m/s}$  which resulted in a Reynolds number of  $2.29 \times 10^6$ . Although the bulk velocity did not match with original experiment it was argued that the Reynolds number can be compared as it would not affect the flow features very significantly.

Bayraktar et al.[6] has used full-scale Ahmed body with a stationary ground for his experimental and CFD investigations at different rear slant angles as well as different yaw angles. He has conducted the experiments on a wide range of Reynolds number and used a curve fitting mathematical equation to obtain the wind averaged drag value. His force coefficients were comparable with the previous experimental studies and also gave a brief insight into vortex shedding of the flow on and around the Ahmed body.

Tural et al.[7] conducted experimental studies on the effect of slant angles for critical,sub-critical and super-critical angles using PIV technique for flow field measurements to observe instantaneous and time-averaged wake flow characteristics.

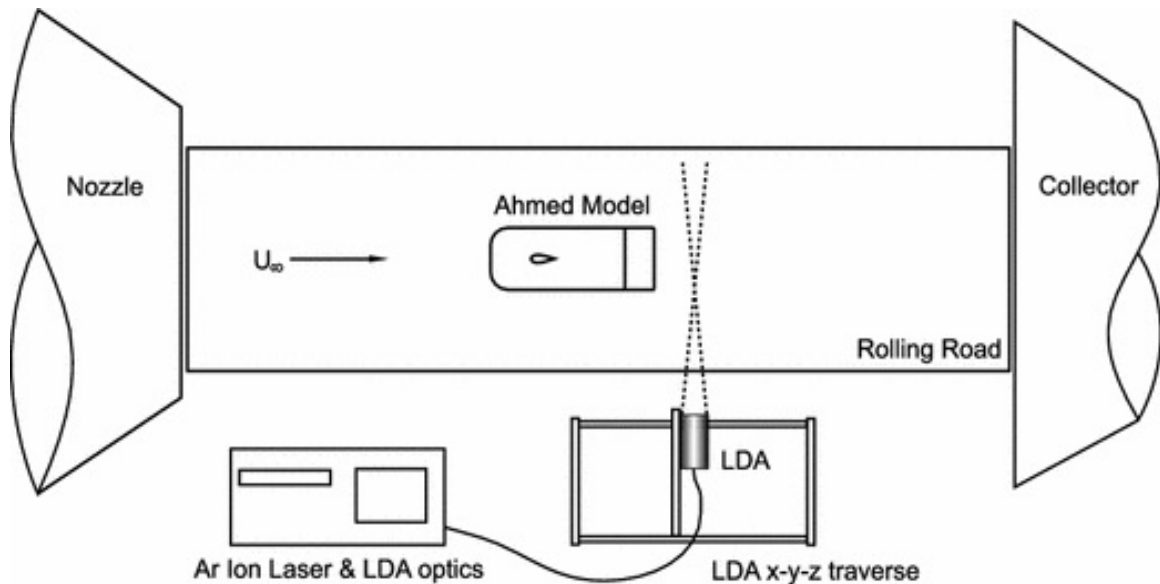


Figure 2.3: Experimental setup of an Strachan[8].

Strachan et al.[8] in his experiments in a moving ground wind tunnel and used LDA technique for the flow field measurements. Strachan used a free stream velocity of 25 m/s which resulted in a Reynolds number of  $1.72 \times 10^6$ . They have used an aerodynamic strut from the roof to mount the Ahmed body in the wind tunnel as shown in Figure 2.3, instead of using stilts at the bottom. The flow fields were compared against the experimental data of Lienhart[5] and the LDA measurements showed a similar trend.

## 2.1 CFD investigations on Ahmed body

The abundance of experimental data and the simplicity of the geometry characterized the Ahmed body as an ideal test case for CFD validation studies. Several turbulence models were tested using these models with an objective of validating the experimental data of Lienhart and Becker[5]. Initial validations are done on a half body without the supporting struts to reduce the cell count. Recent studies used a Full body with supporting struts to reproduce exact flow features.

Krajnovic and Davidson[9] conducted a Large Eddy Simulation (LES) with Ahmed body. He used a Mesh with smallest possible cell size close to Kolmogorov length scale

which predicts the force coefficients accurately. One of the main drawbacks of their study is that they haven't analyzed the effect of Reynolds number on the flow.

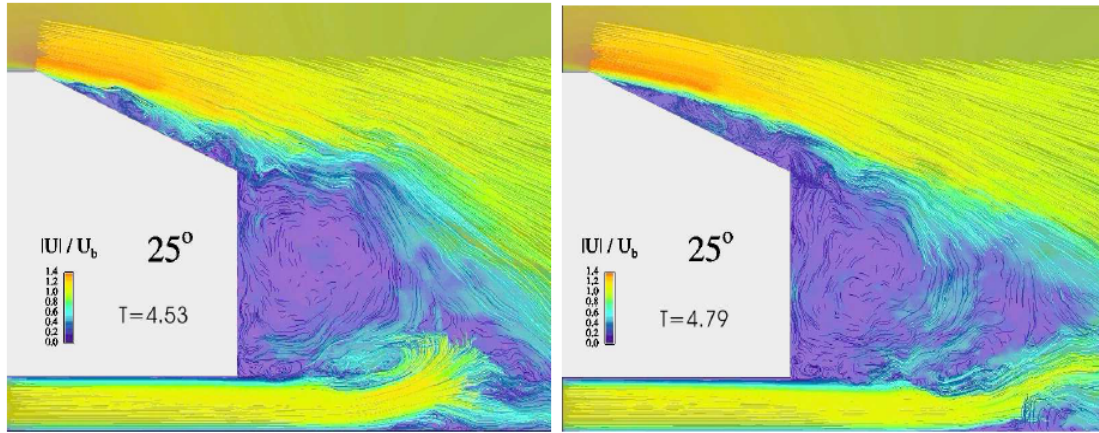


Figure 2.4: Instantaneous flow field of LES of Hitenburg[10].

Eric Serre et. al[11] conducted an LES with Spectral Vanishing Method. This method was able to predict the separation and reattachment in good agreement with the experimental value along with a good level of turbulence along the downstream of the slant angle. A major drawback for this model is that it overpredicts the value of  $C_d$  by 44%. The reason for this overprediction of the  $C_d$  is due to the presence of a confined recirculation region ahead of the body which essentially increases the cross-sectional area thus resulting in a higher  $C_d$ .

Guilmineau[12] studied the flow characteristics using DES-SST and RANS models for their simulations. DES overpredicted the separation over the slant and slightly predicts the occurrence of side wall vortices. His DES model over-predicted the  $C_d$  value by 15%. His RANS model completely failed to match the experimental data because of the separated flow on the slant. however, the results for 35-degree slant angle matched well with experimental values.

Ashton et al.[13] performed CFD studies using the RANS and DDES variants of SST  $k-\omega$  model. His studies showed that the RANS models failed to predict the size of the recirculation region irrespective of the mesh resolution, modeling level and the

choice of length scale. The main reason for this failure is that the RANS models underpredict the turbulence levels on the slant which resulted in the overprediction of the separation region. On the other hand, DDES performed better when compared to the RANS with good mesh resolution. He further improved the DDES model by injecting the synthetic turbulence upstream of the separation point in order to provide correct turbulence levels on the onset of separation.

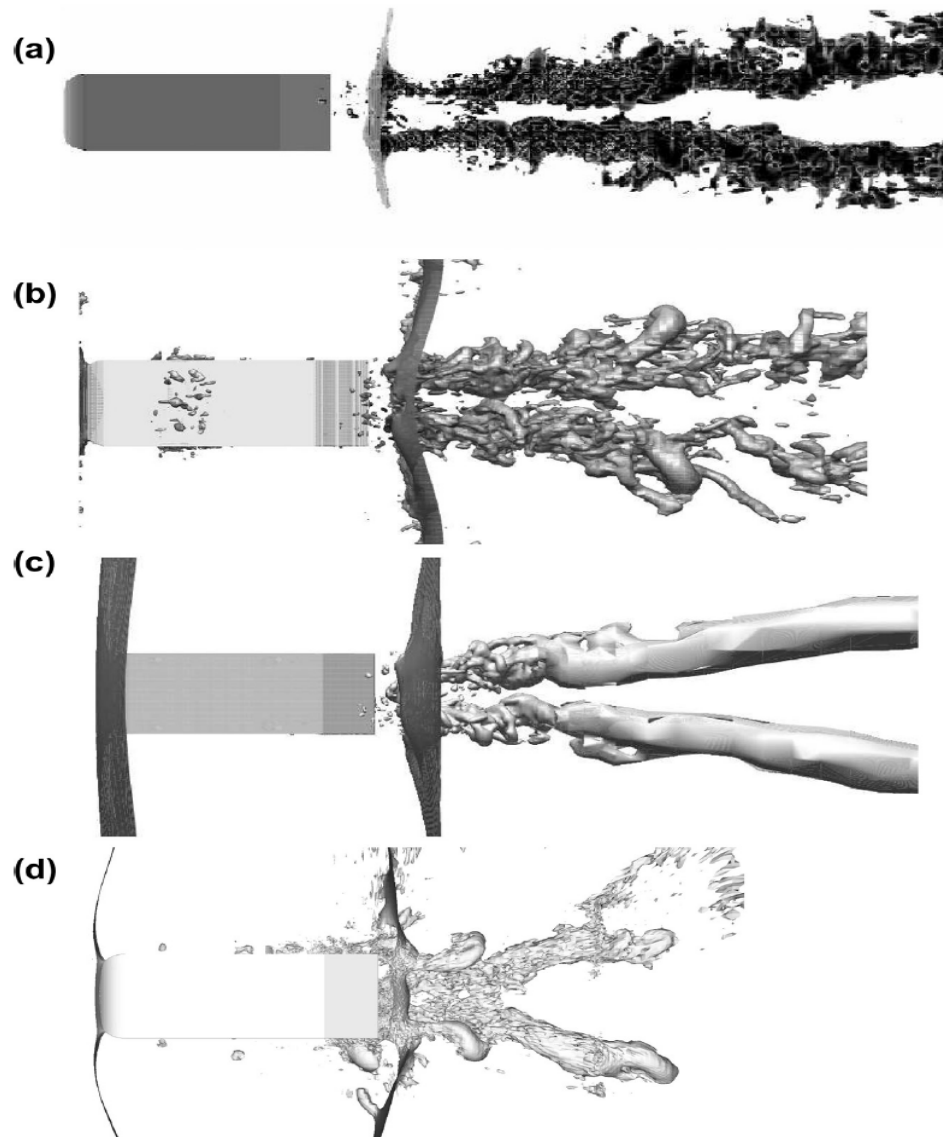


Figure 2.5: Instantaneous Iso-surfaces of pressure displaying the wake expansion and the resolution of turbulence[11]: (a) LES with near wall modeling, (b) LES-Spectral Vanishing Method, (c) DES-SST, (d) LES-Near Wall Resolution

Maduta et al.[14] conducted RANS computations for the Ahmed body with 25 deg slant angle and used a Reynolds stress model (RSM) for their study. They analyzed the performance of the baseline version and later he modified the baseline version by adding an additional term to the specific dissipation term thus enhancing the turbulence intensity in the early separated shear layer and correctly reproduced the complex flow topology of the Ahmed body.

## CHAPTER 3: Turbulence Modeling

Most of the flows in nature are turbulent, for example, boundary layer flows and wakes flows are turbulent in nature. As stated by Tennekes & Lumley[15], it is very difficult to give a precise definition of turbulence, but it has a number of characteristic features given by Lars Davidson[16].

1. Irregularity – The turbulent flows are irregular, random and chaotic in nature. The flow consists of larger eddies based on flow geometry and smaller eddies due to the presence of viscous forces.
2. Diffusivity – Turbulent flows have high diffusivity, which results in the increase of momentum exchange in boundary layers and thereby delays the separation at bluff bodies (cars).
3. Large Reynolds numbers – In general, the turbulent flow occurs at high Reynolds numbers. For example, the transition from laminar flow to turbulent flow occurs at  $Re$  2300 for pipe flows and at  $Re$  100000 for boundary layers.
4. Three-Dimensional – These flows are three- dimensional, but when these equations are averaged over time then they can be treated as two dimensional.
5. Dissipation – The turbulent flow is dissipative and the transfer of energy takes place from larger eddies to smaller eddies.
6. Continuum – Turbulence is a continuum phenomenon which is governed by the equations of fluid dynamics, this is because the smallest eddies (scales) that are present in the flow are larger than the molecular length scales.

### 3.1 Turbulence Modeling

Turbulence Modeling is one of the key elements in computational fluid dynamics (CFD). In general, the fluid motion is governed by the Navier Stokes equation. The presence of nonlinear terms in the Navier-Stokes equation makes it very difficult to predict the nonlinear behavior and hence it becomes very difficult to obtain a closed solution. This is popularly known as "The Closure Problem". Turbulence modeling is a technique to close the mean flow equations by making a few assumptions and finding the solution numerically. The main objective of the Turbulence models is to solve the Navier-Stokes equations directly by modeling the fluid flow using simpler methods.

$$\frac{\partial u_i}{\partial x_i} = 0 \quad (3.1)$$

$$\frac{\partial u_i}{\partial t} + u_j \frac{\partial u_i}{\partial x_j} = -\frac{1}{\rho} \frac{\partial p}{\partial x_i} + \frac{\partial \tau_{ij}}{\partial x_j} \quad (3.2)$$

$$\tau_{ij} = \mu \left( \frac{\partial u_i}{\partial x_j} + \frac{\partial u_j}{\partial x_i} \right) \quad (3.3)$$

Equation 3.1 represents conservation of mass while Equation 3.2 represents the conservation of momentum and Equation 3.3 represents viscous stresses,  $\tau_{ij}$  [17] and are in incompressible form.

In the automotive field, the effects of fluctuating quantities have huge importance, and many turbulence models have been developed to focus on particular aspects to get accuracy and at the same time save computational time and money.

### 3.2 Classification of Turbulence Models

Depending on the complexity of flow and its level of resolving, the turbulence models are broadly classified into three categories;

- Direct Numerical Simulations (DNS)
- Large Eddy Simulation (LES)
- Detached Eddy Simulation (DES)
- Reynolds Averaged Navier Stokes (RANS)

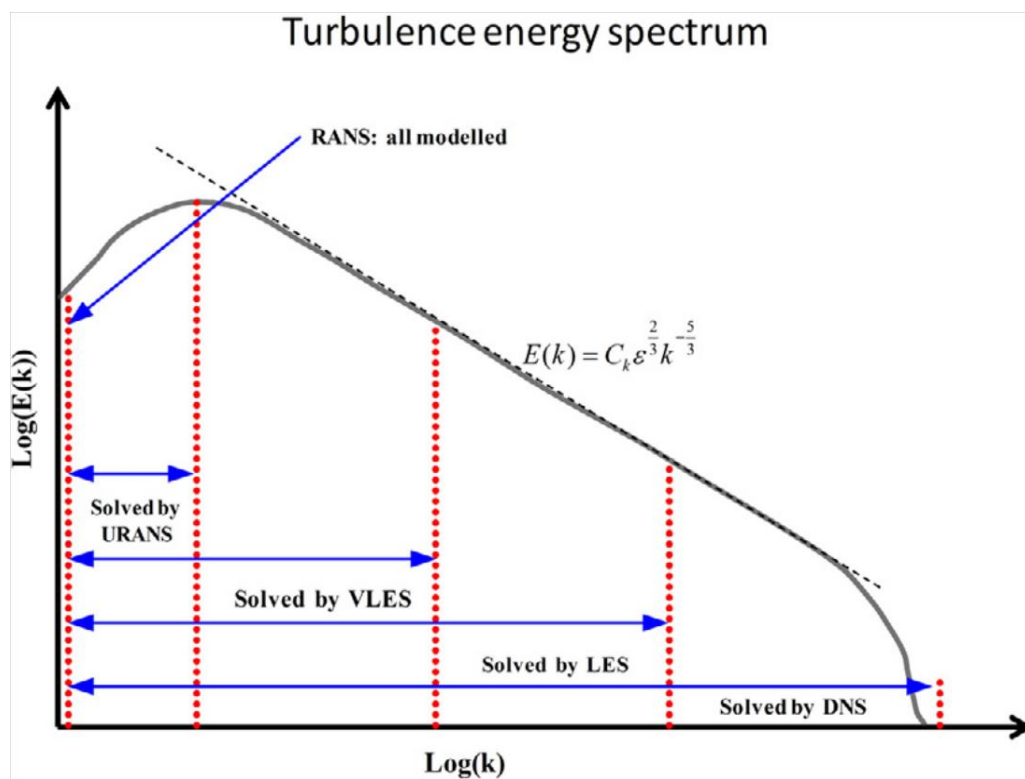


Figure 3.1: Turbulence Energy Spectrum[18].

Turbulence energy spectrum from the Figure 3.1 gives a brief idea about the level of resolving of the individual turbulence models.

#### 3.2.1 Direct Numerical Simulation (DNS)

In DNS the Navier Stokes equations are solved numerically without involving turbulence modeling. This way of solving the flow needs resolved temporal and spatial

scales of turbulence. This method requires the highest computational power and time when compared to any other model. It requires grid points proportional to  $Re^{\frac{9}{4}}$ . This method is applied only for low Reynolds numbers with highly refined mesh. In case of a car simulation with a minimal amount of turbulence, the number of grid points required is  $10^{18}$ , which makes it impractical to use in vehicle aerodynamics as of now, but in near future, this can be possible with the increase in computational power.

### 3.2.2 Large Eddy Simulation (LES)

LES has wider acceptability than RANS because of its accuracy and less computational time required when compared to the DNS (Direct Numerical Simulation). In the LES approach, the large-scale models are filtered using Navier- Stokes equations and the small scales are developed using the SGS (Sub Grid Scale) model. The LES approach is highly useful for the investigation of the turbulence at high Reynolds numbers. The SGS stress tensor which is symmetric plays an important role in the dynamic coupling of large and small eddies. The accuracy of the LES model is dependent on the SGS modeling. The most common selection of the SGS model is based on the eddy viscosity model. One of the best models is the Smagorinsky model referred in[18], This model has many drawbacks such as failing to predict the inverse energy transfer, turning of Smagorinski constant ( $C_s$ ). A modified version of this model is known as Lilly model, which reduces the errors in the constant was developed by Germano as referred by C.D. Argyropoulos[18]. The main advantage of this method is that it yields good results in the near wall regions.

### 3.2.3 Detached Eddy Simulation (DES)

The DES (Detached Eddy simulation) was modeled to handle the massively separated flow with high Reynolds number, especially for the fields of aerospace and automotive. DES combines RANS and LES depending on the turbulent length scale and grid spacing. DES treats the boundary layer regions with RANS and the mas-

sively separated particles with LES. The drawback of this model is that it is dependent on the grid construction, especially in the region of transition between RANS to LES.

### 3.2.4 Reynolds Averaged Navier Stokes (RANS)

RANS is a simpler technique in which the turbulent scales are averaged over time. Since this is an averaged method it lacks accuracy where there are more complex flows such as vortex Shedding, large separation zones, and high streamlined curvature[19]. In particular, RANS depends on an implicit assumption that there will be scaled separation between all the turbulent scales of the flow and will be replaced with statistical models. The RANS models are used widely because of their short turn over time and are not computationally expensive when compared to DNS or LES.

### 3.3 Choice of Turbulence model for the study

The selection of turbulence model mainly depends on the level of description, completeness, cost, and ease of use and the required level of accuracy for analyzing the flow field. A wide variety of turbulence models are available depending on their use and applicability. For steady-state simulations, Reynolds Averaged Navier-Stokes(RANS) turbulence modeling is employed. One equation, two equation, and Reynolds stress models come under the RANS modeling.

Now we will see in brief how these models are established. As we know that the fluid flow equations are governed by Navier-Stokes equations.

$$\frac{\partial \tilde{u}_i}{\partial \tilde{x}_i} = 0 \quad (3.4)$$

$$\frac{\partial \tilde{u}_i}{\partial t} + \tilde{u}_j \frac{\partial \tilde{u}_i}{\partial \tilde{x}_j} = \frac{1}{\rho} \frac{\partial}{\partial x_j} \tilde{\sigma}_{ij} \quad (3.5)$$

In equation 3.5,  $\tilde{\sigma}_{ij}$  is the stress tensor and is a combination of  $\tilde{p}$  (hydrodynamic pressure),  $\mu$  (dynamic viscosity) and  $\tilde{s}_{ij}$  (rate of strain) :

$$\tilde{\sigma}_{ij} = -\tilde{p}\delta_{ij} + 2\mu\tilde{s}_{ij} \quad (3.6)$$

$$\tilde{s}_{ij} = \frac{1}{2} \left( \frac{\partial u_i}{\partial x_j} + \frac{\partial u_j}{\partial x_i} \right) \quad (3.7)$$

The term  $\tilde{\sigma}_{ij}$  is known as Reynolds stress tensor which is symmetric and thus has six components which leads to the closure problem.

Two equation eddy viscosity models are widely studied in the literature. From the onset of these models, several studies tried to improve their performance and efficiency. The  $k - \epsilon$  turbulence model of Launder and Spalding[20] performs well when applied to turbulent shear flows but it in the near wall boundary layer, as it poorly detects the adverse pressure gradients. The original  $k - \omega$ [21] turbulence model has superiority to  $k - \epsilon$  model as it performs better in the near wall region, but this model is highly sensitive to the free stream. Mentor's Shear Stress Model (SST)[22][23] is a combination of both these models, which has the advantages of the both. The SST model uses  $k - \omega$  in the near wall region and  $k - \epsilon$  in the free stream and the switching is controlled by a blending function. The SST model is widely used in the automotive industry. Even though it has many advantages, this model has some shortcomings. Literature shows that the  $k - \omega$  SST model fails in predicting the flow features of the Ahmed body with a slant angle ( $\phi = 25$  deg) of Ahmed body. This model is selected for the study in this thesis to evaluate its performance and to improve its shortcomings.

The baseline equations of the SST turbulence model are as follows

$$\frac{\partial(\rho k)}{\partial t} + \frac{\partial(\rho u_j k)}{\partial x_j} = P - \beta^* \rho \omega k + \frac{\partial}{\partial x_j} \left[ (\mu + \sigma_k \mu_t) \frac{\partial k}{\partial x_j} \right] \quad (3.8)$$

$$\frac{\partial(\rho\omega)}{\partial t} + \frac{\partial(\rho u_j \omega)}{\partial x_j} = \frac{\gamma}{\nu_t} - \beta^* \rho \omega^2 + \frac{\partial}{\partial x_j} \left[ (\mu + \sigma_\omega \mu_t) \frac{\partial \Omega}{\partial x_j} \right] + 2(1 - F_1) \frac{\rho \sigma_{\omega 2}}{\omega} \frac{\partial k}{\partial x_j} \frac{\partial \omega}{\partial x_j} \quad (3.9)$$

$$P = \tau_{ij} \frac{\partial u_i}{\partial x_j} \quad (3.10)$$

$$\tau_{ij} = \mu_t \left( 2S_{ij} - \frac{2}{3} \frac{\partial u_k}{\partial x_k} \right) - \frac{2}{3} \rho k \delta_{ij} \quad (3.11)$$

$$\mu_t = \frac{\rho a_1 k}{\max(a_1 \omega, \Omega F_2)} \quad (3.12)$$

The transport equations for Turbulent kinetic energy ( $k$ ) and Specific dissipation rate ( $\omega$ ) are given by Equations 3.8 and 3.9.

The coefficients for the model are calculated from the blending function  $F_1$ , such that each coefficient  $\phi$  is given by:

$$\phi = F_1 \phi_1 + (1 - F_1) \phi_2 \quad (3.13)$$

The coefficients for the set 1 ( $\phi_1$ ) are

$$\beta_1 = 0.0750, \sigma_{k1} = 0.85, \sigma_{\omega 1} = 0.5, \kappa = 0.41, \gamma_1 = \frac{\beta_1}{\beta^*} - \sigma_{\omega 1} \frac{\kappa^2}{\beta^*}$$

The coefficients for the set 2 ( $\phi_2$ ) are

$$\beta_2 = 0.0828, \sigma_{k2} = 1.0, \sigma_{\omega 2} = 0.856, \kappa = 0.41, \gamma_2 = \frac{\beta_2}{\beta^*} - \sigma_{\omega 2} \frac{\kappa^2}{\beta^*}$$

for both set 1 and set 2

$$\beta^* = 0.09, \alpha = 1$$

Since the RANS turbulence model neglects the effects of the unsteady motion of the flow, which affects the wake of the flow. As a part of the investigation, we have selected the IDDES variant of the SST model to study the unsteady motions. This model is a hybrid of RANS and LES where it uses RANS in the near wall region and

LES in the regions away from the wall. The switch between the RANS and LES is governed by a damping function. The modification to the SST model for IDDES is by replacing the specific dissipation term with

$$\tilde{\omega} = \frac{\sqrt{k}}{l_{HYBRID}\beta^* f_{\beta^*}} \quad (3.14)$$

where,  $f_{\beta^*}$  is the free-shear modification factor and  $l_{HYBRID}$  is the hybrid length scale determined based on the effective length scale and the local grid size using a blending function and an elevating function.

$$C_{DES} = C_{DES,k-\omega}F_1 + C_{DES,k-\epsilon}(1 - F_1) \quad (3.15)$$

where  $C_{DES,k-\epsilon} = 0.61$  and  $C_{DES,k-\omega} = 0.78$ .

Even though this model is better than the RANS models, the DES-SST model has shortcomings in predicting increased dissipation when the grid scale is less than the turbulent scale. This model is further improved to correct this overprediction. Delayed Detached- Eddy model is an improved version of the DES-SST model where the transition from RANS to LES is done as a function of the ratio of local turbulent length sales to grid spacing which results in delaying of dissipation when compared to DES formulation. A further development of DDES is the Improved Delayed Detached- Eddy Simulation (IDDES). IDDES switches between DDES and wall modeled LES depending on the amount of grid resolution in the near wall region and the amount of local turbulence. IDDES has several filters and switching functions in addition to adding the Wall - modeled LES (WMLES) capability[24].

## CHAPTER 4: NUMERICAL SETUP

This chapter gives a detailed numerical setup of the simulations carried out in this thesis and the mesh used for the study. Initially, the simulations are carried out with commercial finite volume code, STAR-CCM+ 11.04 and later moved to STAR-CCM+ 12.06. All simulations were performed using Reynolds Averaged Navier Stokes (RANS) and Improved Delayed Detached Eddy Simulations (IDDES) variants of SST  $k - \omega$  model.

### 4.1 Ahmed body model

The model used in this study is the Ahmed reference model with different slant angles. Preliminary validation of the setup is done using the Ahmed body with  $25^\circ$  slant angle as seen from the Figure 4.1. The model has the dimensions 1044 x 389 x 288 (mm). This model is created in SolidWorks and later into StarCCM+ as a CAD file.

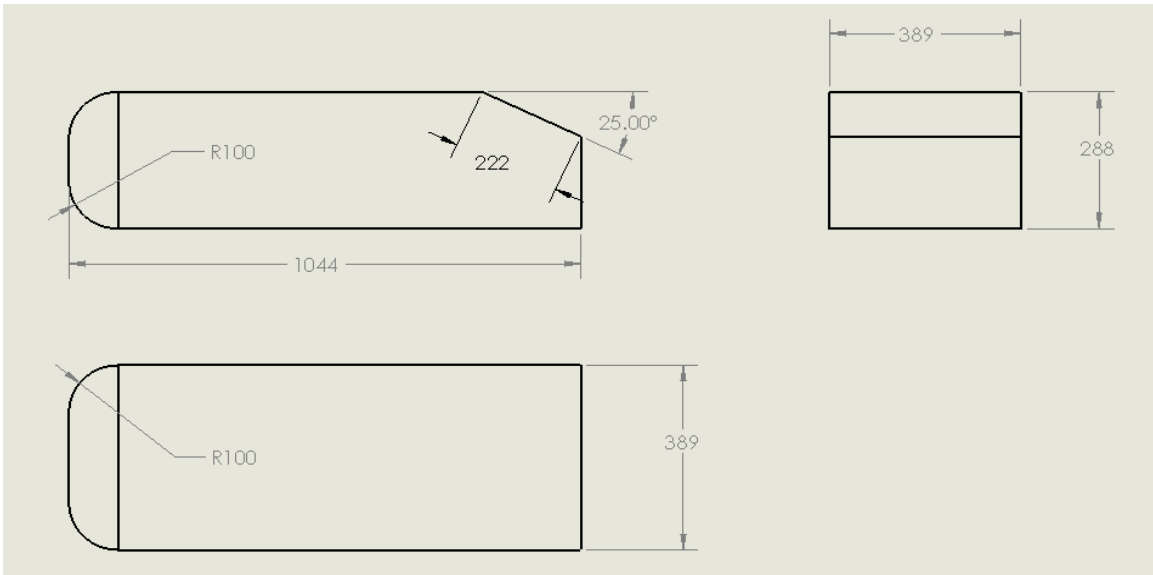


Figure 4.1: Schematic diagram of Ahmed body used in this study.

## 4.2 Mesh Setup

The discretization of the domain into smaller sub-domains is known as Meshing. Mesh plays a significant role in the computational results, the presence of one bad cell may lead to the propagation of the wrong solution throughout the domain. We are using STAR-CCM+ for preparing the surface and volume mesh for the simulations.

The value of the wall  $y^+$  is important for accurate prediction of the flow at the boundary layer. Ideally, a wall  $y^+$  of 1 is recommended. From the definition of wall  $y^+$ , the first node height can be estimated, where  $\rho$  is density,  $U$  is the free stream velocity and  $\mu$  is dynamic viscosity as shown in Equation 4.1

$$y^+ = \frac{\rho U y}{\mu} \quad (4.1)$$

The wall  $y^+$  aimed for these simulations is 0.1 which resulted in the first node height of 0.001 mm.

In order build a mesh that suits the transient IDDES simulations, the Taylor microscale ( $\lambda$ ) was estimated by using the Equation 4.2 as given in Tennekes and Lumley[15], where  $A_1$  is an undetermined constant set to 0.5,  $Re$  is the Reynolds number and  $L$  is the Length scale. The  $\lambda$  value obtained is used to drive the grid spacing required to resolve the majority of the eddies.

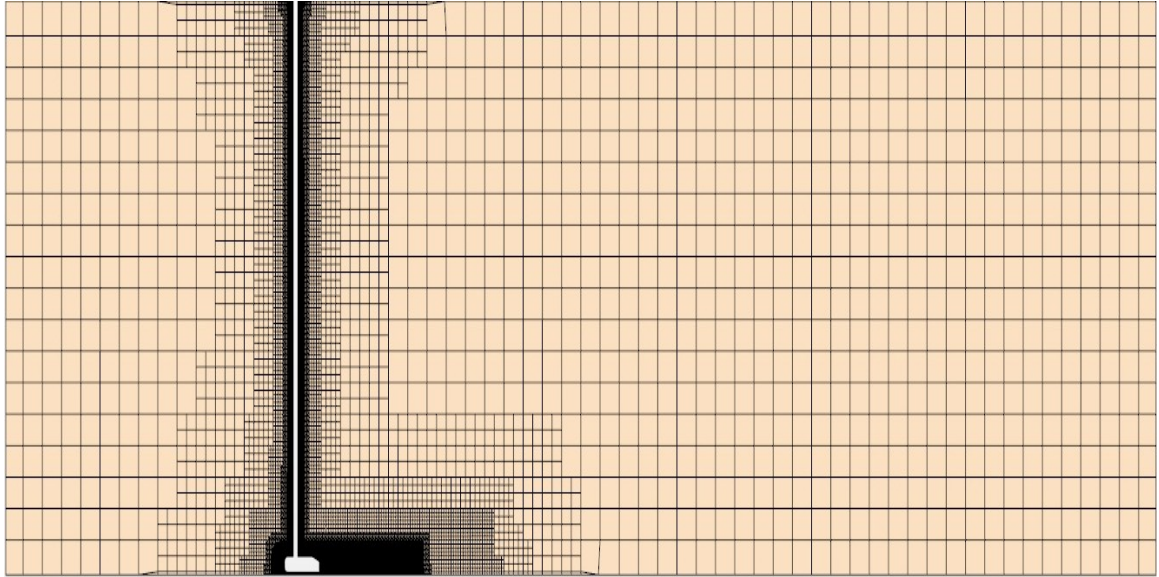
$$\lambda = \sqrt{15} \frac{1}{\sqrt{A_1}} \frac{1}{\sqrt{Re}} L \quad (4.2)$$

The Taylors micro scale for the current simulations is approximately 3 mm. For the IDDES simulations, the approximated Taylor micro scale was resolved near the body.

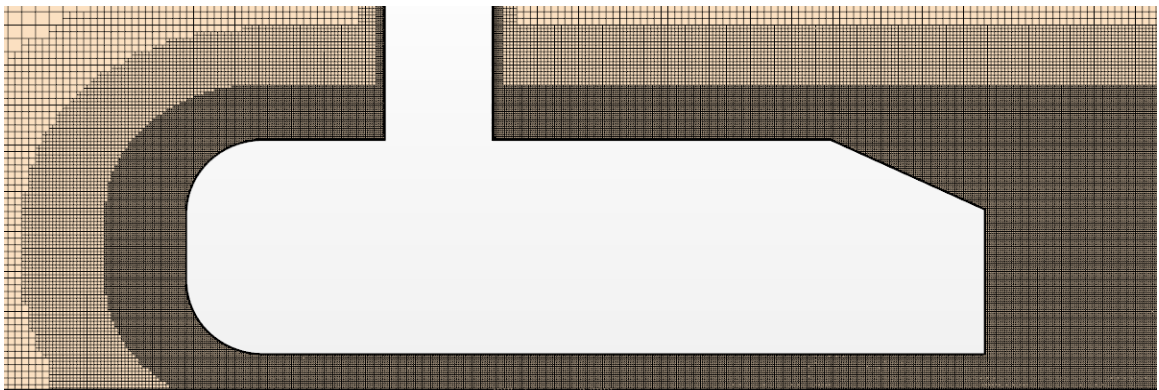
The building of the core mesh completely depends on the surface mesh. The surface of the Ahmed body was split into four different surfaces and part curves were also computed for the body. Surface controls have been used to ensure the proper surface

mesh distribution over the Ahmed body. Once the surface mesh has been established, the core mesh has been developed over the surface mesh. Trimmed cells are used for building the volume mesh. In order to ensure the resolving of the flow around the Ahmed body, volume sources have been used. Three levels of volume refinements have been used near the Ahmed body, the closest being with cell size less than the Taylor's length scale. The primary volume source is stretched  $0.1 \times L$  in normal and  $0.5 \times L$  in the lateral direction. The secondary volume source is stretched  $0.2 \times L$  in normal and  $2 \times L$  in the lateral direction and the third volume source is stretched  $0.4 \times L$  in normal and  $4 \times L$  in the lateral direction. Prism layers are added on the surface of the body in order to capture the boundary layer.

A mesh independence study has been performed and the results are shown in the table(5) of the Results chapter. From that study, the base size of 2.25 mm has been selected and is kept constant throughout the simulations. For the preliminary study of the turbulence closure coefficient parameters, the overhead support sting has been neglected for the simplification of the problem. For the validation of the optimum set of closure coefficients the support sting has been included as seen from the Figure ???. The support sting was modeled using an aspect ratio of  $t/c = 0.15$  and a chord length of 140 mm. The wake of the support sting is not completely resolved as it is computationally expensive.



(a) Distant view



(b) Zoomed view

Figure 4.2: Mesh scenes of the domain with the overhead sting at  $Y=0$ .

A virtual wind tunnel was prepared with the dimensions of  $35 L \times 10 L \times 10 L$ , which results in a negligible blockage ratio. The inlet is  $8L$  ahead of the body so that the flow becomes steady before it reaches the body and the outlet is  $26 L$  from the rear end of the Ahmed body so that the wake can be resolved effectively.

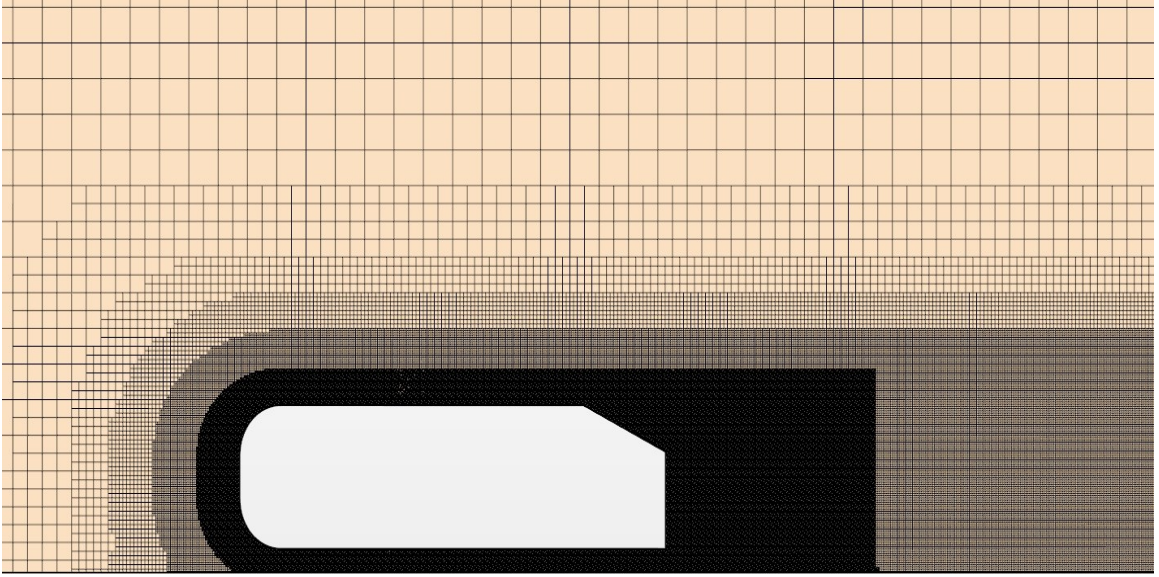


Figure 4.3: Mesh scenes of the domain without the overhead sting at  $Y=0$ .

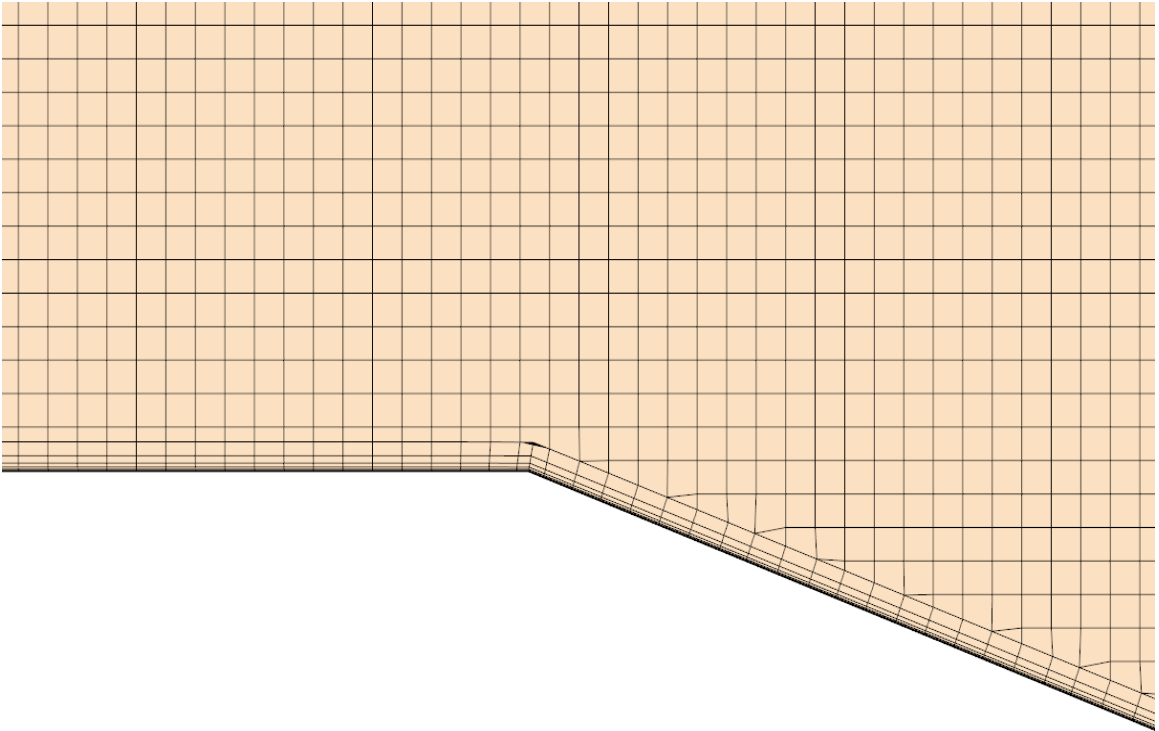


Figure 4.4: Mesh scene near the rear slant in the plane  $Y=0$ .

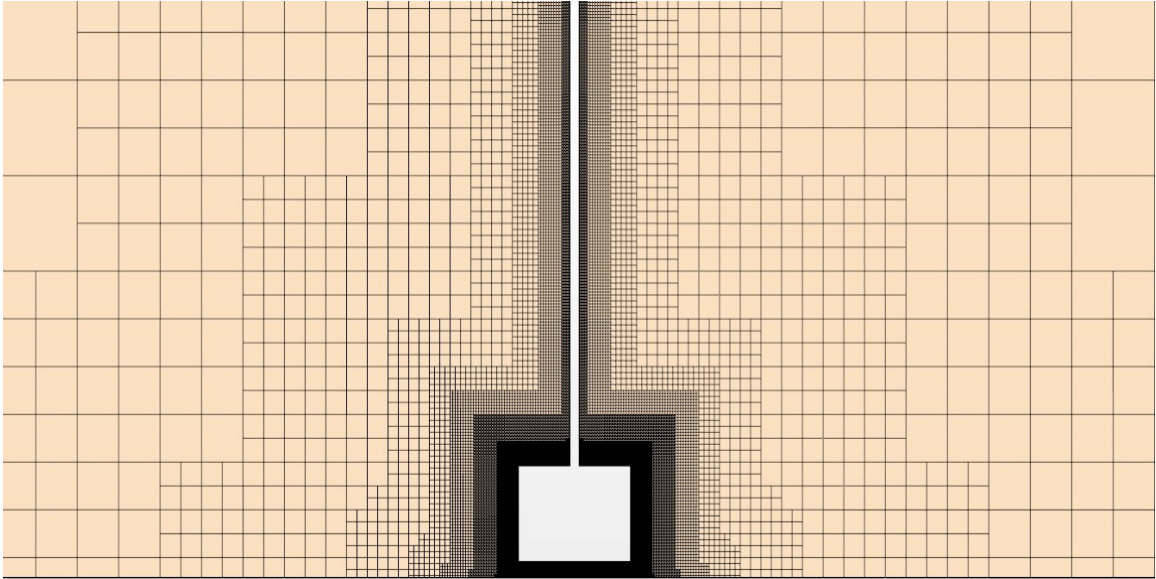


Figure 4.5: Mesh scenes of the domain with the overhead sting at  $X=0$ .

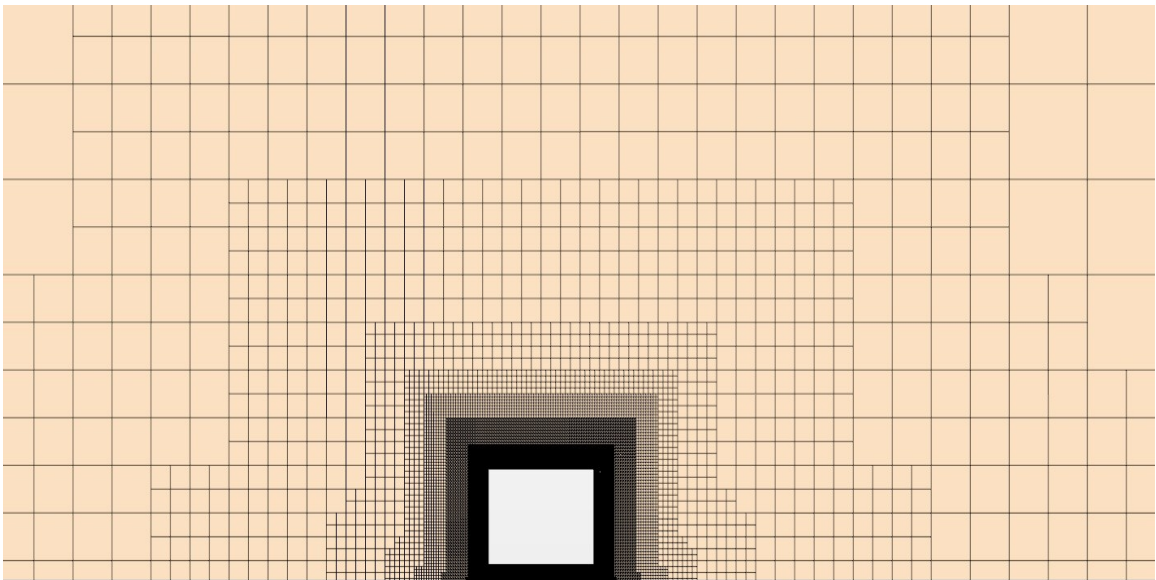
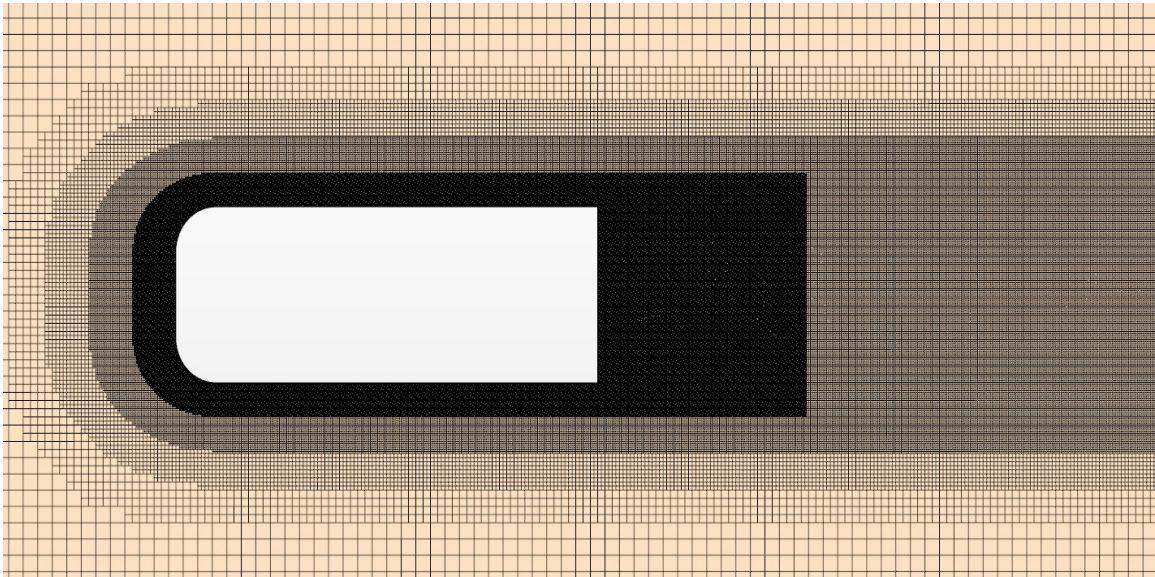


Figure 4.6: Mesh scenes of the domain without the overhead sting at  $X=0$ .

Detailed Meshing parameters have been given in the Table 4.1 and the several sectional views of the mesh is presented in the Figures 4.2, ??, 4.6, 4.5, 4.7 and 4.4.

Table 4.1: Mesh parameters used in the simulations.

Mesh Parameters	Value
Base Size	18 mm
Smallest cell size	2.25 mm
No.of prism layers	12
Prism layer thickness	2 mm
First node height	0.001 mm

Figure 4.7: Mesh scenes of the domain at  $Z=0$ .

### 4.3 Boundary conditions

The specification of the boundary conditions is as crucial as the mesh setup because the initial values for propagating the solution are taken from the boundaries. Incorrect boundary specification may lead to a poor prediction of the results. The boundary conditions chosen for this simulation are inlet as velocity inlet with a value of 25 m/s. This velocity was used by Strachan[25] in his experiment which is the validation experimental data for this thesis, the outlet is set to pressure outlet, the ground is defined as no-slip wall and the ground motion is specified through tangential velocity

specification. The top and side walls of the domain are modeled as symmetry planes. The boundary conditions are the same for the both steady-state RANS and Transient IDDES simulations.

Table 4.2: Boundary conditions used in the simulations.

Boundary	Type
Inlet	Velocity Inlet
Outlet	Pressure Outlet
Ground	No-Slip wall
Side walls	Symmetry Plane
Top	Symmetry Plane

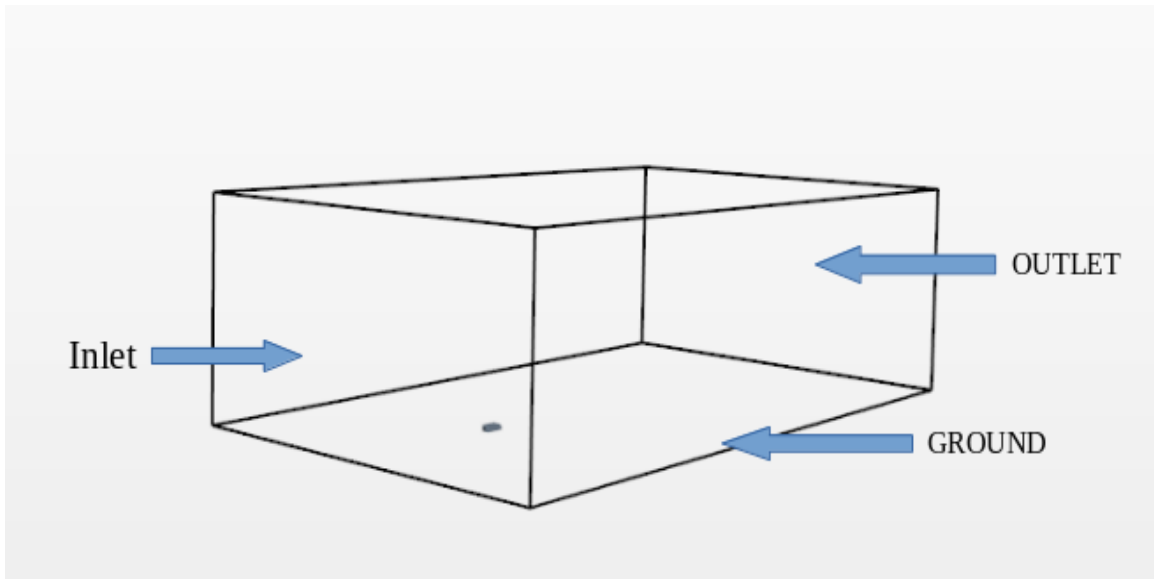


Figure 4.8: Computaional Domain with boundary conditions

#### 4.4 Physics Setup

The physics setup of the simulations is relatively simple as there are no moving or rotating parts. The initial conditions for the setup are  $\rho = 1.205 \text{ kg}/m^3$  and  $\mu = 1.82 \times 10^{-5} \text{ N}\cdot\text{s}$ . The free stream velocity is set to  $25 \text{ m}/s$  which resulted in a Reynolds number of  $1.72 \times 10^6$ .

Table 4.3: Physics setup for the steady state RANS simulations.

Type	Model
Space	3 dimensional
Time	Steady
Material	Gas
Solver	Segregated flow solver
Equation of State	Constant Density
Viscous Regime	Turbulent
Reynolds-Averaged Turbulence	SST $k - \omega$
Wall distance	Exact wall distance

The steady-state RANS simulations are run for 10,000 iterations and the convergence is monitored using the  $C_d$  and  $C_l$ . For the steady state, the Force coefficients are averaged over the last 2000 iterations.

For the IDDES simulations, the implicit unsteady solver is used for the numerical computations with (fill here with more details) The time step chosen for the simulation was  $9 \times 10^{-5}$  which resulted in a CFL number of 1. The simulations are run for a total physical time of 2 seconds that took a computer wall time of approximately 4 days on 96 cores with 8 Gb per core. The data is averaged over the last 0.72 seconds (4000-time steps) of physical time. All the force coefficients are recorded to observe the solution convergence.

Table 4.4: Physics setup for the IDDES simulations.

Type	Model
Space	3 dimensional
Time	Implicit Unsteady
Material	Gas
Solver	Segregated flow solver
Equation of State	Constant Density
Viscous Regime	Turbulent
Detached Eddy Simulation	SST $k - \omega$
Wall distance	Exact wall distance

## CHAPTER 5: Results and Discussions

### 5.1 Mesh Independence Study

In the mesh independence study, the RANS turbulence model was chosen over the IDDES turbulence model as RANS requires a shorter time for the convergence. All the simulations have been performed on half body geometry as Ahmed body is symmetric about the center plane. The choice of the geometry with half body over the geometry with the full body can be seen from the Table 5.1 Case 1 represents half body simulation and Case 2 represents full body simulation. The change in  $C_d$  and  $C_l$  is 1 count, but the cell count is double for the full body simulation. In order to save computational time and resources the mesh independence study as shown in Table 5.2 is carried out using half body geometry. In addition, the overhead sting used in the Strachan's[8] experiment has been excluded in this study for simplification, as the sting has an airfoil profile and it requires more mesh refinement and adds to the expense of computational power and time.

Table 5.1: Variations of  $C_d$  and  $C_l$  for Half body and Full body simulations.

Case	Smallest cell Size	Total Cell count	$C_d$	$C_l$
1	2.25 mm	19 M	0.254	0.073
2	2.25 mm	38 M	0.255	0.074

In order to use the same mesh for the IDDES simulations, the Taylors Microscale based on Re of  $1.72 \times 10^6$  is approximately 3 mm as given in Equation 4.2. The study has been done starting from the Taylors length scale and repeated for cell sizes less than the Taylors length scale.

Table 5.2: Variations of  $C_d$  and  $C_l$  for different cell sizes.

Case	Smallest cell Size	Total Cell count	$C_d$	$C_l$
a	3 mm	10 M	0.250	0.0313
b	2.5 mm	15 M	0.251	0.043
c	2.25 mm	19 M	0.254	0.073
d	2 mm	28 M	0.255	0.072
e	1.9 mm	32 M	0.255	0.071
f	1.85 mm	35 M	0.256	0.069

From the Table 5.2 we can see that  $C_d$  keeps on increasing as the cell size decreases. For cases with a cell size of 2mm and 1.9 mm there is no change in the  $C_d$  value and the lift decreases by 0.4 % and from the cases with a cell size of 2mm and 1.9 mm the change in  $C_d$  and  $C_l$  is 0.4 %. This change is small and can be neglected and as there is a significant change in the Total cell count, the present author chooses 2.25 mm as the smallest cell size for the optimized mesh.

## 5.2 Effect of closure coefficients on the force predictions

An optimized mesh has been generated based on the Mesh independence study as shown in Table 5.2. The turbulence model tested in this thesis is the SST  $k - \omega$  turbulence model. The baseline case has been completed with the default coefficients and the results are tabulated in the Table 5.3

Table 5.3: Variations of  $C_d$  and  $C_l$  for Baseline case compared against experimental data of Strachan[8].

	$C_d$	$C_l$
Baseline	0.254	0.073
Experimental	0.300	0.280
$\Delta$	-15.3%	-73.9%

As seen from the Table 5.3 the baseline case underpredicts the drag and lift coefficient by 15.3% and 73.9% respectively. The huge lift under prediction is due to the flow separation over the rear slant beginning and failure to reattach completely over the slant. RANS models underestimate the Turbulent Kinetic Energy (TKE) over the rear slant which results in the overprediction of the size of separation bubble on the slant, that causes failure in reattachment of flow over the slant.

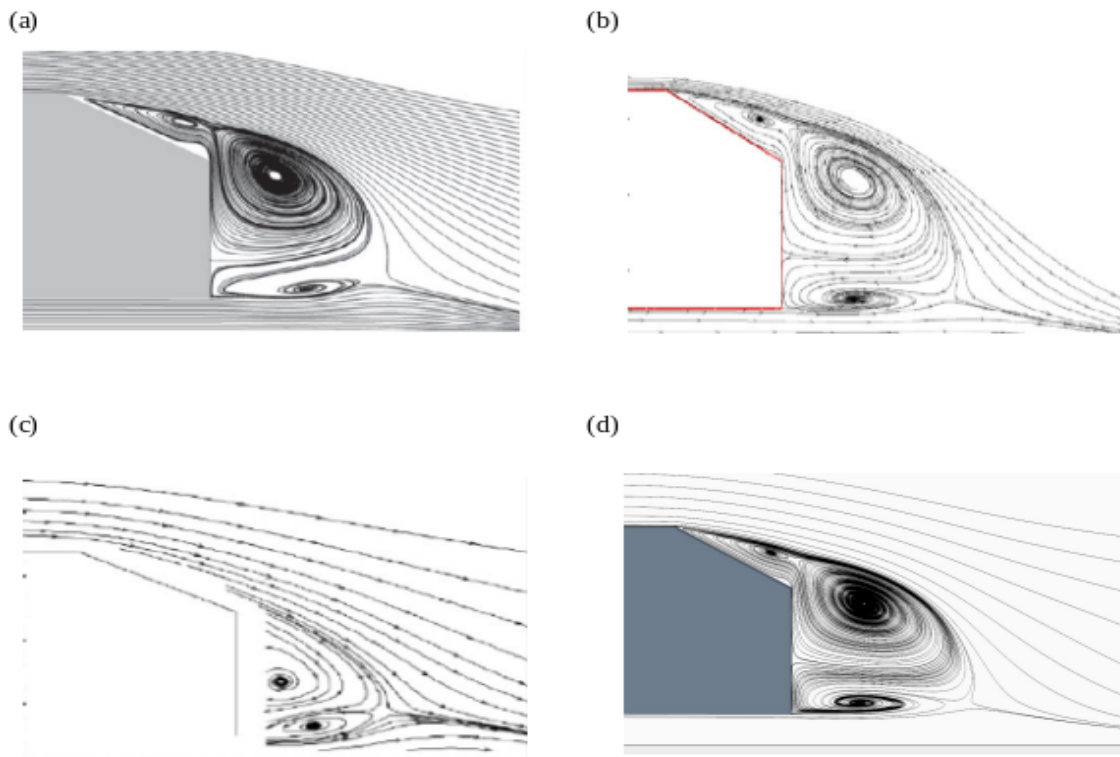


Figure 5.1: Comparison of flow predictions of SST turbulence model from the CFD studies conducted by (a) URANS-SST of Ashton et al.[13], (b) RANS-SST of Guilmineau et al.[12], (c) Experiment of Lienhart[5], (d) Current Baseline SST

From the Figure 5.1 the SST  $k - \omega$  model clearly overpredicts the size of the separation bubble on the slant and in the wake. The current baseline SST predicts the flow features similar to the CFD work of Ashton et al.[13] and Guilmineau et al.[12]. This encouraged the present author to investigate the poor performance of the SST model in predicting the flow features for the ever challenging 25deg rear slant angle.

The investigation was started from the formulation of the  $k - \omega$  model[21]. This model is essentially a two-equation model and is developed based on dimensional analysis and has unknown double and triple correlations. These unknown correlations cause the closure problem in the formulation of these models. This problem was solved by replacing the correlations with closure coefficients.

The  $k - \omega$  model has six closure coefficients. The closure coefficients mainly influence the production, dissipation, diffusion and cross-diffusion terms of the Transport equations as seen in the Equations 3.8 and 3.9. These coefficients are not exact and set to assure the observed turbulence properties of the canonical flows. For instance, the ratio of  $\beta_*$  to  $\beta$  is established by applying the  $k - \omega$  model to a decaying homogeneous, isotropic turbulence[19].

As these closure coefficients are set from the features observed from simple canonical flows, it is highly likely that these coefficients would not work for the automotive flows as they have separations and reattachments. This motivated the present author to modify the closure coefficients with a motto of improving the flow predictions.

However one should be aware that these coefficients cannot be modified randomly. There are some limitations and necessary conditions that these closure coefficients should satisfy in order to obey the physics of the flow. The coefficient  $C_{\epsilon 1}$  should never be greater than  $C_{\epsilon 2}$ , as it makes the term to be the source instead of sink. In the  $k - \omega$  model, the value of  $\beta_*$  should not be greater than because the model becomes the standard  $k - \epsilon$  model. The von-Karman constant  $\kappa$ , which is a function of  $C_{\epsilon 1}$  and  $C_{\epsilon 2}$  as shown in Equation should not exceed 0.41

$$\kappa^2 = \sigma_{\epsilon} C_{\mu}^{\frac{1}{2}} (C_{\epsilon 2} - C_{\epsilon 1}) \quad (5.1)$$

The present modifications in this thesis are based on strictly following these limitations and restrictions.  $\beta_*$ ,  $\sigma_{\omega 1}$ ,  $\sigma_{\omega 2}$  are the closure coefficients that have been studied extensively in this thesis. The closure coefficients  $\sigma_{k 1}$  and  $\sigma_{k 2}$  have not studied exten-

sively as the influence was not that great when compared to the closure coefficients mentioned earlier.

For the closure coefficients study the baseline mesh has been used and the closure coefficients are modified one at a time, keeping the other coefficients at the default value. A total of 20 simulations have been performed for which the the force coefficients have been recorded and tabulated in the Tables 5.4, 5.5, 5.6 respectively.

Table 5.4: Variations of  $C_d$  and  $C_l$  for different values of  $\sigma_{\omega 1}$ .

Case	1	2	3	4	5
$\sigma_{\omega 1}$	0.4	0.45	0.5	0.55	0.6
$C_d$	0.251	0.252	0.254	0.256	0.258
$C_l$	0.066	0.069	0.073	0.078	0.083

Table 5.5: Variations of  $C_d$  and  $C_l$  for different values of  $\sigma_{\omega 2}$ .

Case	1	2	3	4	5
$\sigma_{\omega 2}$	0.8	0.856	0.9	0.1	1.05
$C_d$	0.251	0.254	0.260	0.267	0.270
$C_l$	0.053	0.073	0.087	0.111	0.120

Table 5.6: Variations of  $C_d$  and  $C_l$  for different values of  $\beta^*$ .

Case	1	2	3	4	5
$\beta^*$	0.07	0.08	0.09	0.10	0.11
$C_d$	0.261	0.258	0.254	0.256	0.264
$C_l$	0.176	0.090	0.073	0.076	0.028

For better understanding of the data represented in the Tables 5.4, 5.5, 5.6, the  $C_d$  and  $C_d$  are compared against the experimental values and the percentage relative deviation of the CFD from experiment is shown in Figure 5.2 and Figure ??.

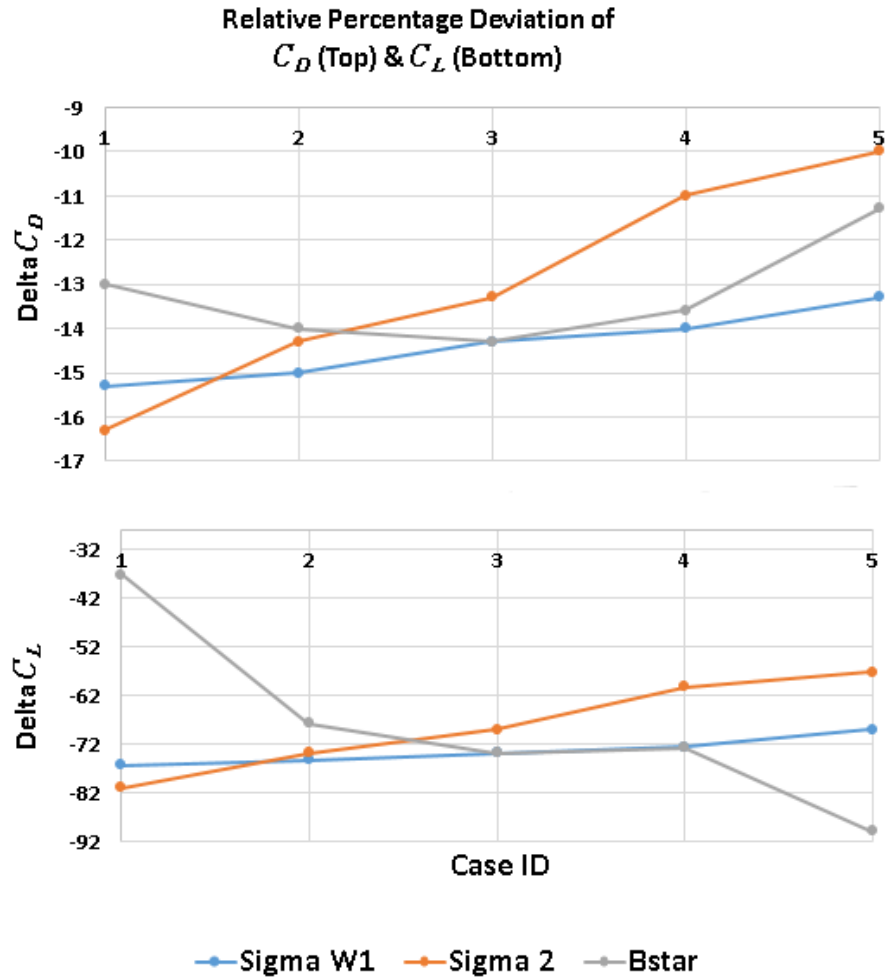


Figure 5.2: Percentage relative deviation of  $C_d$  and  $C_l$  values predicted by CFD to that of experimental values.

From the Figure 5.2 and we can clearly see a linear trend for the force predictions for the closure coefficients  $\sigma_{\omega_1}$  and  $\sigma_{\omega_2}$  as the coefficient value increases the  $C_d$  and  $C_l$  predictions kept moving towards the experimental value. The  $C_d$  prediction of the coefficient  $\beta^*$  follows a trend where decreasing the coefficient and increasing the coefficient increased the  $C_d$  with the smallest value occurring at the default value  $\beta^* = 0.09$  but the  $C_l$  prediction is quite sensitive to the changes and does not show a clear trend.

Among all the closure coefficients that are varied,  $\sigma_{\omega_2}$  has a significant impact in the force predictions when compared to  $\sigma_{\omega_1}$  and  $\beta^*$ , this is because  $\sigma_{\omega_2}$  influences diffusion

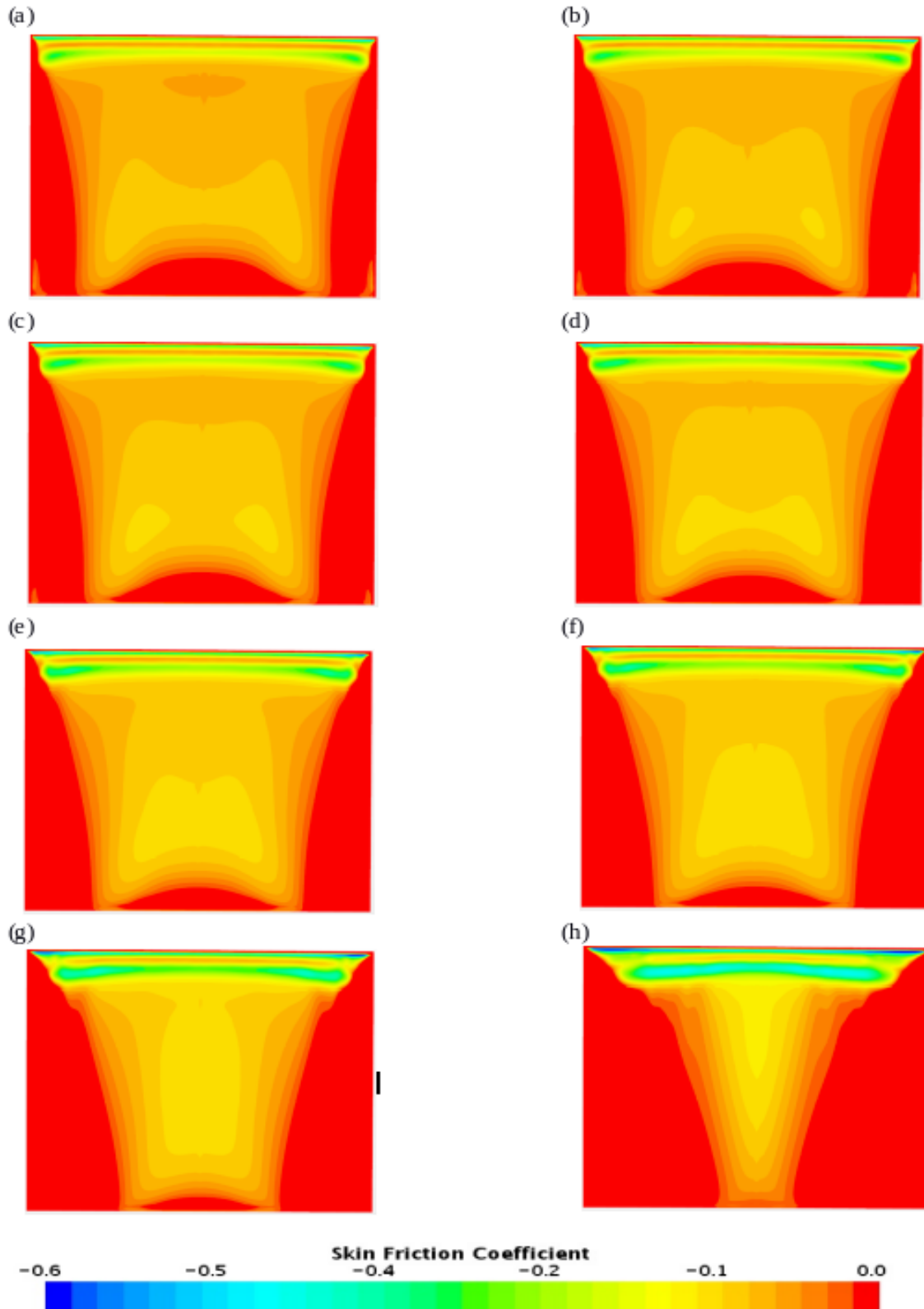
and cross-diffusion terms whereas  $\sigma_{\omega 1}$  affects only the diffusion term. Whereas  $\beta^*$ , on the other hand, affects both production terms in  $k$  and  $\omega$  transport equations, so it acts like a balance between both the terms and hence we are observing a quadratic nature for the prediction of  $\beta^*$ . The current tuning of the coefficients is still far away from the experimental value, so from the trends observed from the above 5.2 and ???. The present author further increased the value of the  $\sigma_{\omega 2}$  value and the  $\sigma_{\omega 2}$  and also studied the combined effects of these closure coefficients. A detailed studied of the flow features has been done for these closure coefficients in order to see how these closure coefficients affecting the flow field.

### 5.3 Effect of closure coefficients on the flow predictions

In this section, we will see how the closure coefficients are affecting the flow features. From the force predictions study in the above section, we could see that  $\sigma_{\omega 2}$  has the highest influence. we now further increased its value and observed the flow features.

In order to assess the performance of the modified coefficients, the analysis began with the drawbacks of the Baseline case. The baseline case overpredicts the separation bubble over the slant and hence there is no reattachment on the slant, but the Experiments show separation and reattachment on the slant. This flow feature can be visualized using the skin friction coefficient over the slant. When we plot skin friction over the slant, the negative values of the skin friction coefficient indicates separation and positive values indicate re-attachment. From the Figure 5.3 we can see the contour plots of Skin friction coefficient over the rear slant for all the modifications of the  $\sigma_{\omega 2}$  parameter. As the value of  $\sigma_{\omega 2}$  increases the size of the recirculation bubble decreases, but still, the flow features do not match the experiments.

The reason for over predicting the size of the separation bubble is due to the underprediction of the TKE over the slant. Figure 5.4 we can see the contours of TKE over the slant. As the  $\sigma_{\omega 2}$  value increases the TKE prediction increases, which helps in getting the separation bubble smaller.



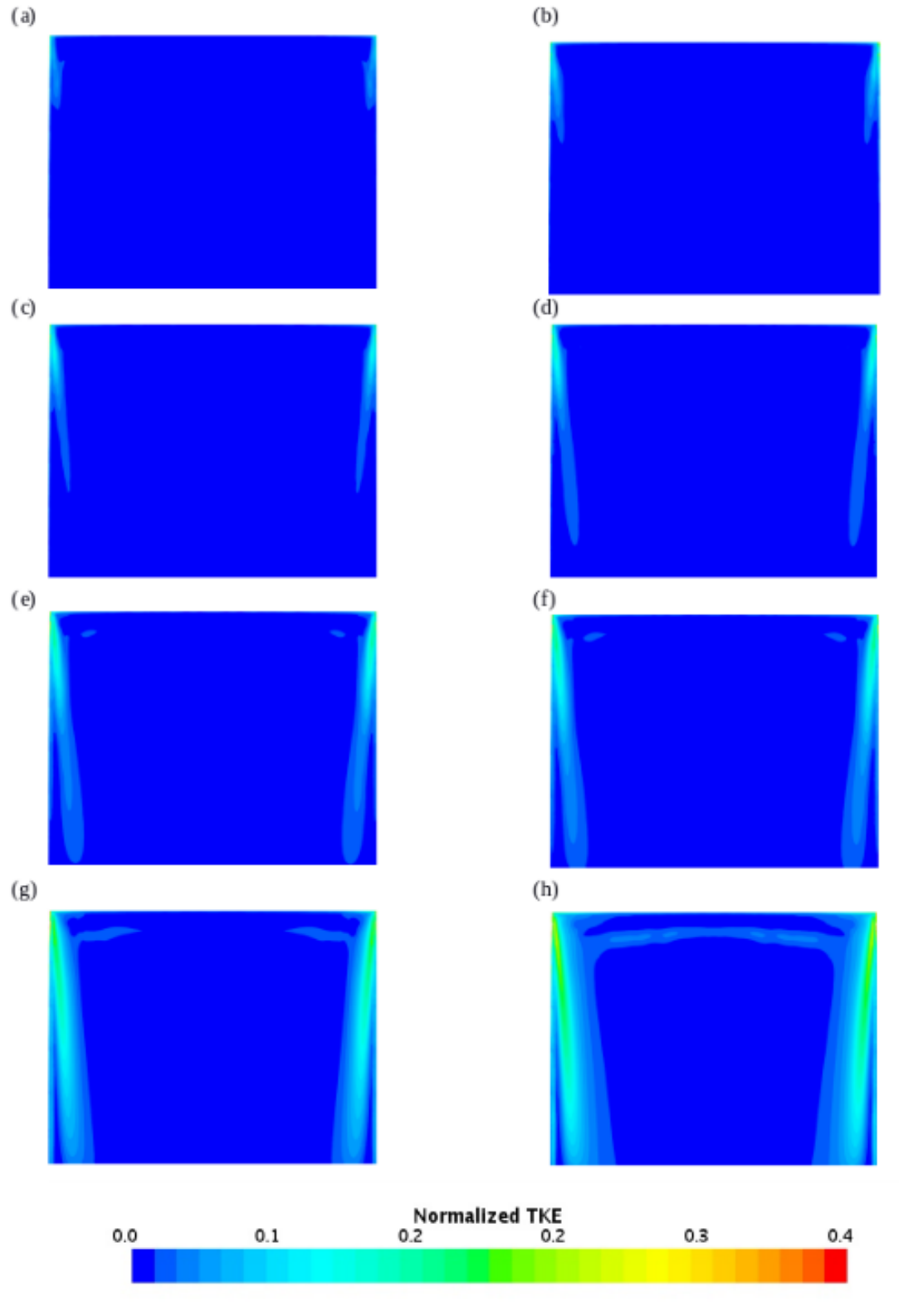


Figure 5.4: Contours of Normalized TKE over the rear slant for different values of  $\sigma_{\omega_2}$ ; sub figures a-h represents  $\sigma_{\omega_2} = 0.8, 0.856, 0.9, 0.956, 1.05, 1.12, 1.36, 1.712$ .

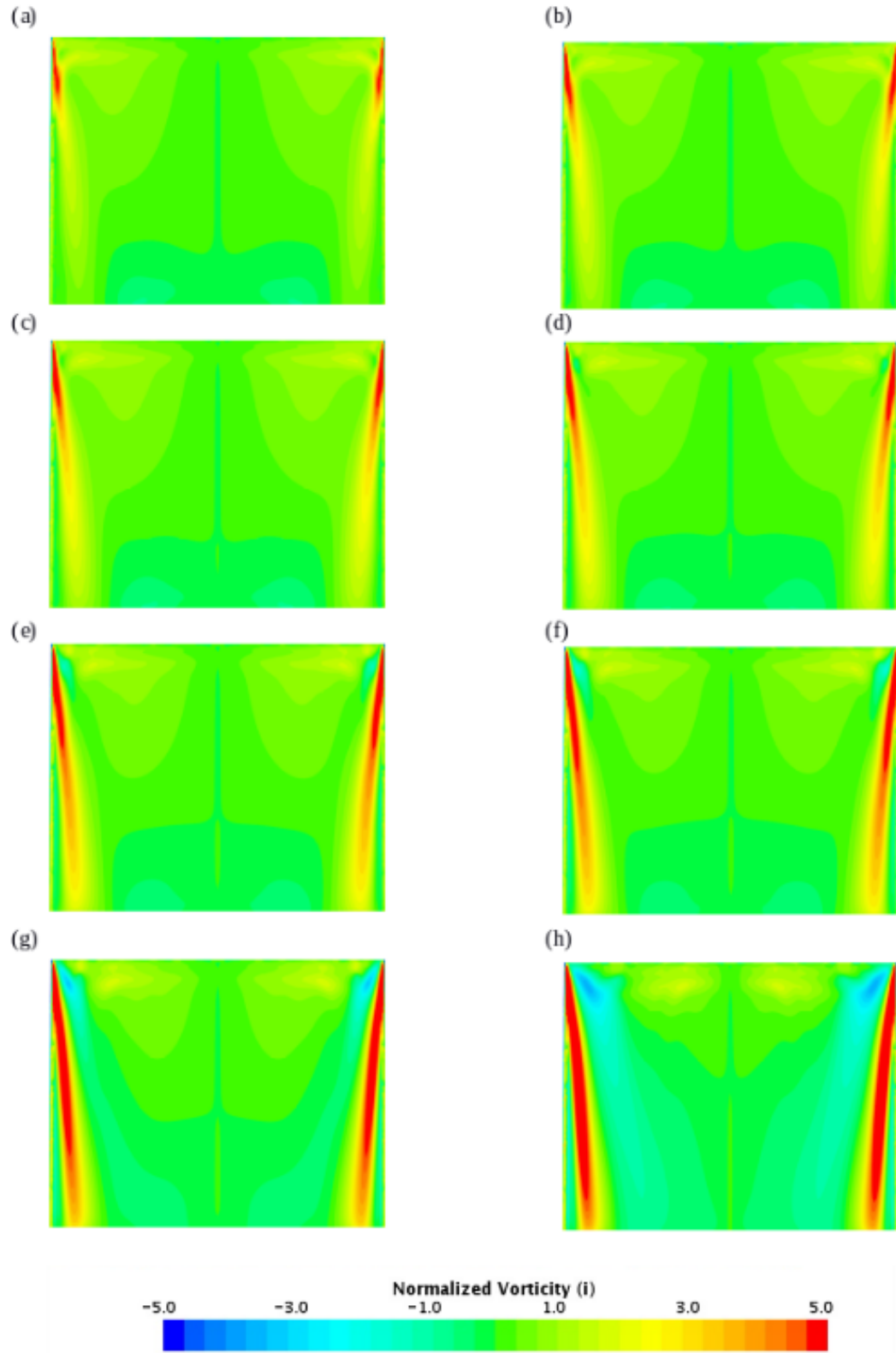


Figure 5.5: Contours of Normalized Vorticity (i) over the rear slant for different values of  $\sigma_{\omega_2}$ ; sub figures a-h represents  $\sigma_{\omega_2} = 0.8, 0.856, 0.9, 0.956, 1.05, 1.12, 1.36, 1.712$ .

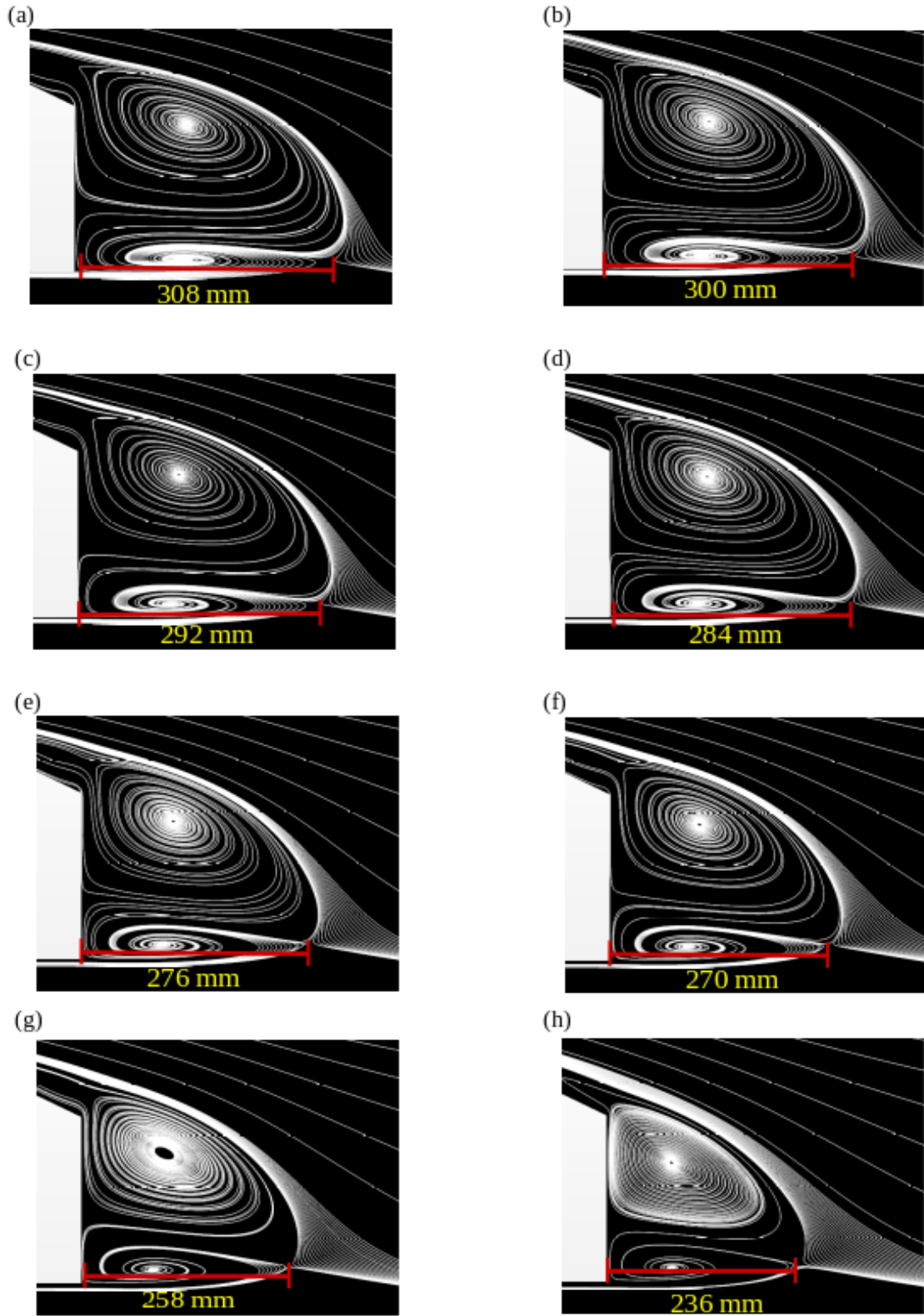


Figure 5.6: Contour of Streamlines in the wake for different values of  $\sigma_{\omega_2}$ ; sub figures a-h represents  $\sigma_{\omega_2} = 0.8, 0.856, 0.9, 0.956, 1.05, 1.12, 1.36, 1.712$ .

The underprediction of TKE also affects the strength of the counter-rotating vortices over the rear slant. In order to analyze this, we have plotted contours of Normalized vorticity (i) component over the slant as shown in Figure 5.5. As the value of  $\sigma_{\omega 2}$  increases the strength of the counter-rotating vortices increases, which helps in getting the flow to reattach up to some extent.

The influence of  $\sigma_{\omega 2}$  parameter can be seen from the 5.6, the flow reattachment in the wake is improved by increasing the value of  $\sigma_{\omega 2}$ . Even though the  $\sigma_{\omega 2}$  coefficient has the highest influence on the flow predictions, it is still not able to reproduce the correct amount of TKE required for the flow to reattach on the slant.

We will now see the Influence of the  $\sigma_{\omega 1}$  parameter on the flow predictions, From the contours of Skin friction coefficient, TKE and Vorticity(i) as shown in Figures 5.7, 5.8 and 5.9. We can clearly observe that the influence of changing the  $\sigma_{\omega 1}$  coefficient is not as significant as the  $\sigma_{\omega 2}$  coefficient.

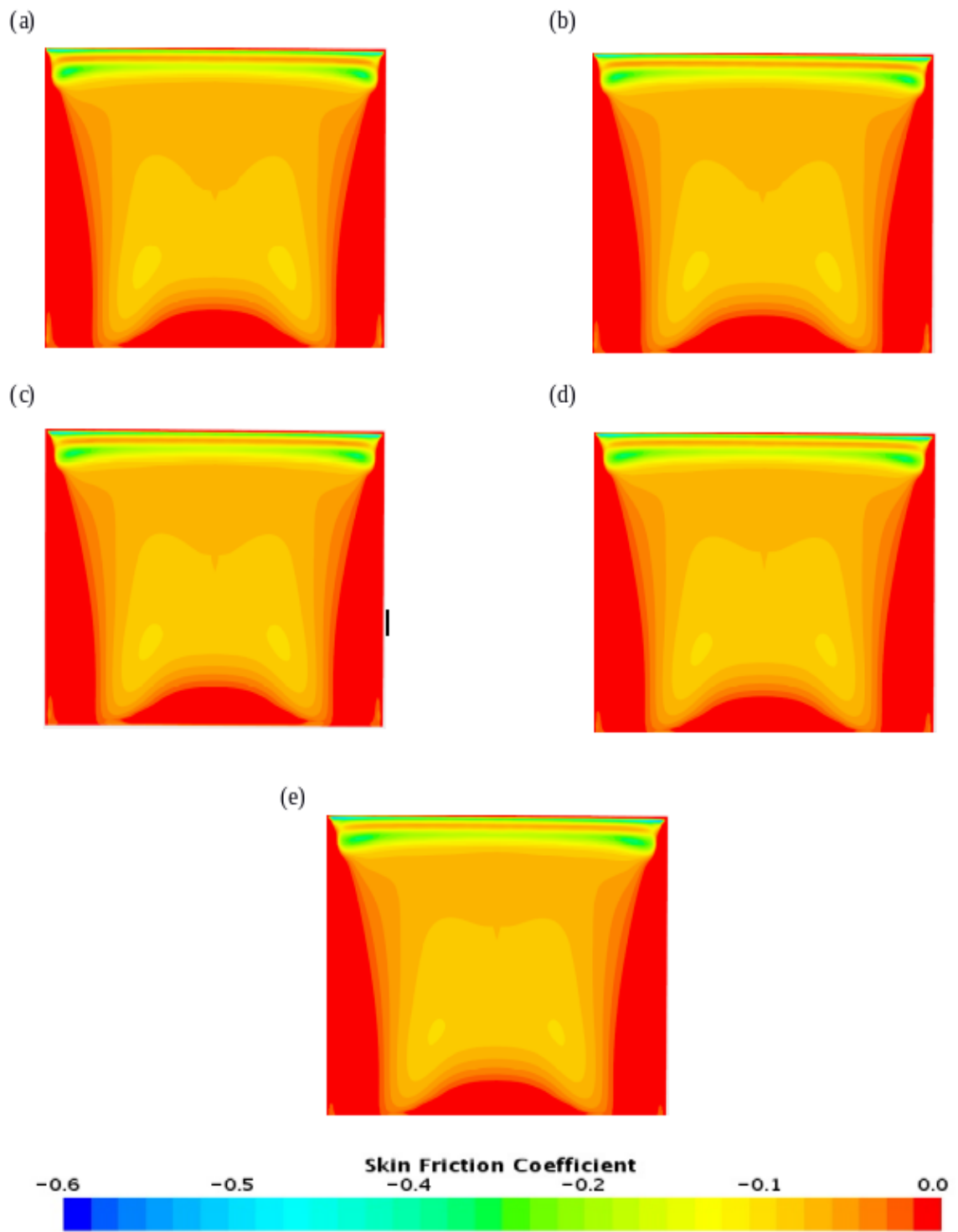


Figure 5.7: Contours of Skin friction coefficient over the rear slant for different values of  $\sigma_{\omega_1}$ ; sub figures a-e represents  $\sigma_{\omega_1} = 0.4, 0.45, 0.5, 0.55, 0.6$ .

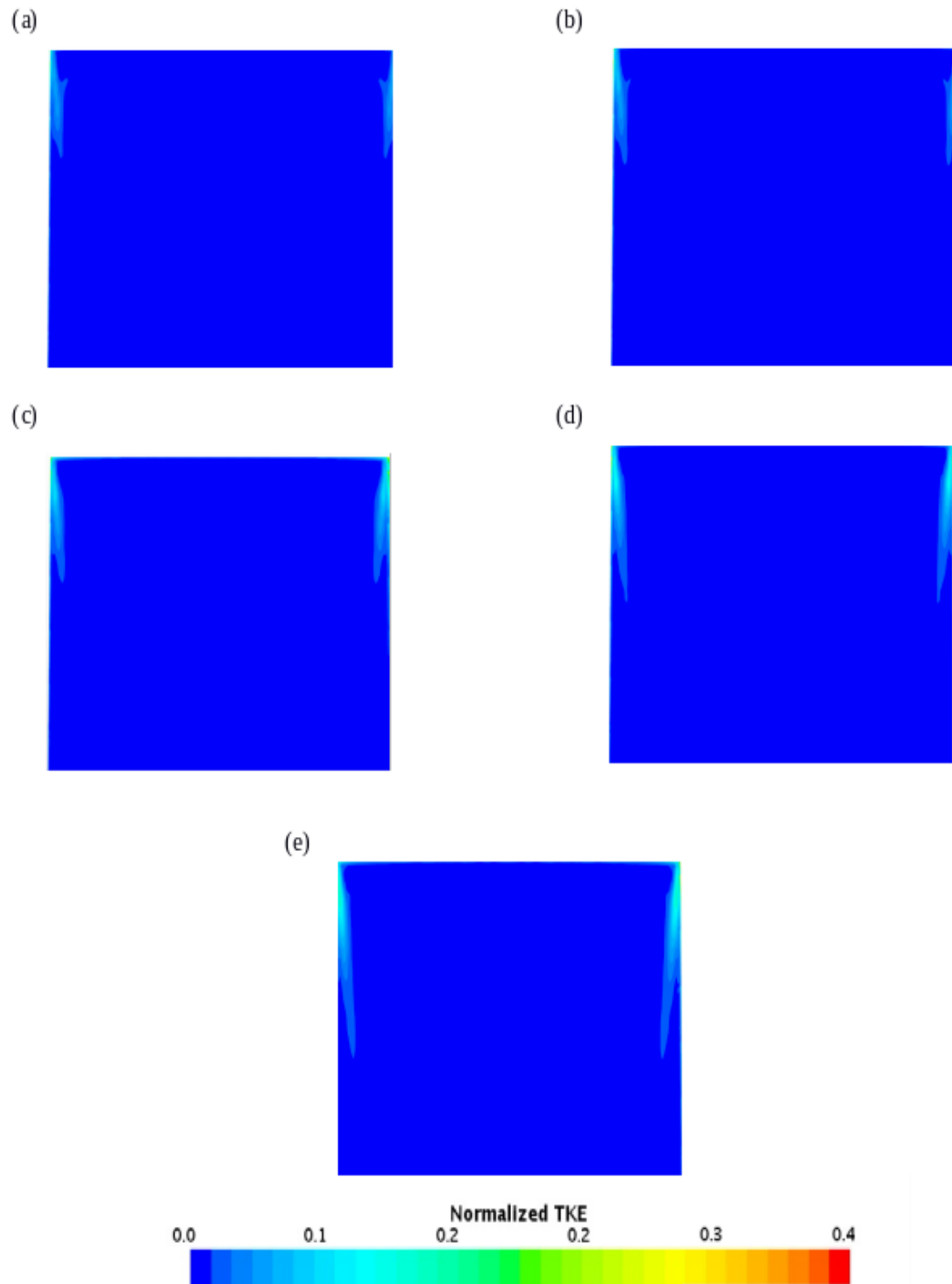


Figure 5.8: Contour of Normalized TKE over the rear slant for different values of  $\sigma_{\omega_1}$ ; sub figures a-e represents  $\sigma_{\omega_1} = 0.4, 0.45, 0.5, 0.55, 0.6$ .

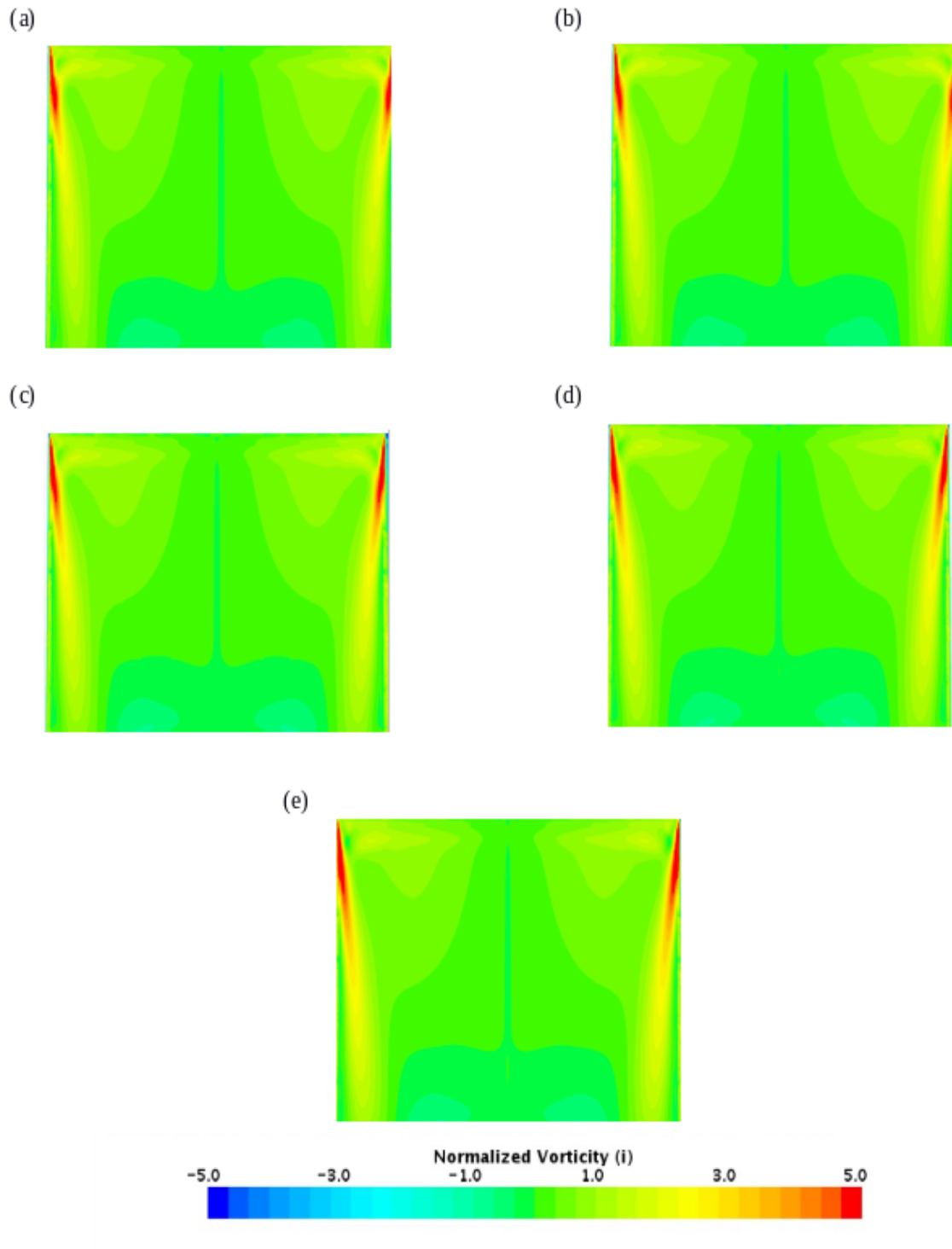


Figure 5.9: Contour of Normalized vorticity (i) over the rear slant for different values of  $\sigma_{\omega_1}$ ; sub figures a-e represents  $\sigma_{\omega_1} = 0.4, 0.45, 0.5, 0.55, 0.6$ .

Since modifying one closure coefficient is still underpredicting the flow predictions, several combinations of closure coefficients were tested to improve the flow predictions. As the closure coefficient  $\sigma_{\omega_2}$  has the highest influence, the value of the  $\sigma_{\omega_2}$  was fixed at 1.712 and the value of  $\sigma_{\omega_1}$  was varied. As seen from the Figure 5.10 The flow predictions improved drastically with increasing  $\sigma_{\omega_1}$  and  $\sigma_{\omega_2}$  together. The flow separation and reattachment can be clearly seen on the slant.

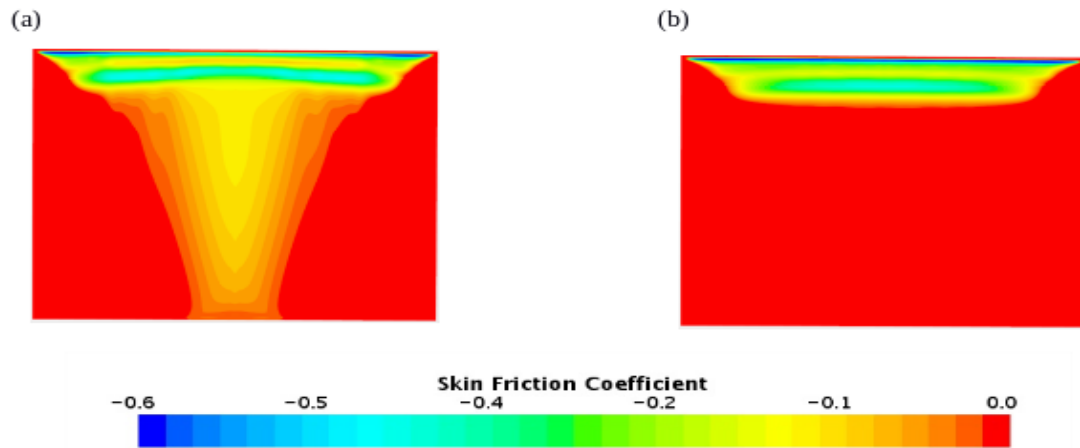


Figure 5.10: Contours of Skin friction coefficient over the rear slant combination of  $\sigma_{\omega_1}$  and  $\sigma_{\omega_2}$ ; sub figures (a) represents  $\sigma_{\omega_1} = 0.5$  and  $\sigma_{\omega_2} = 1.712$  and sub figures (b) represents  $\sigma_{\omega_1} = 0.65$  and  $\sigma_{\omega_2} = 1.712$

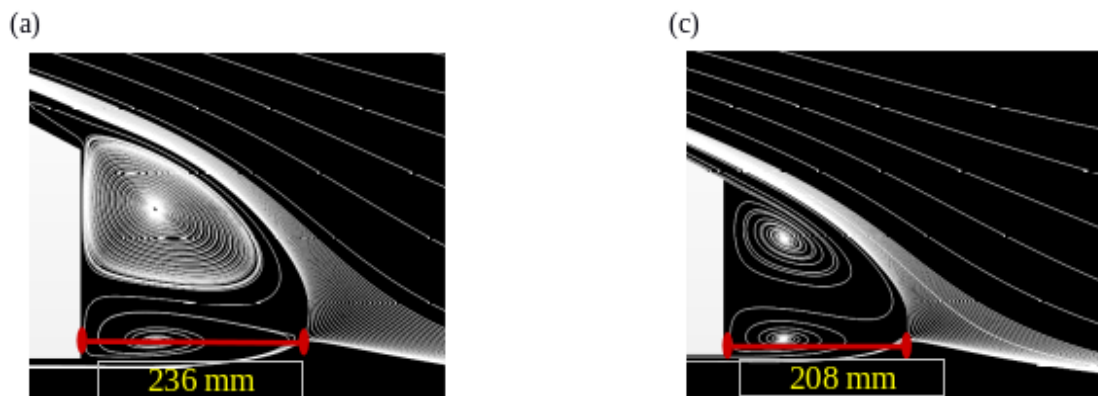


Figure 5.11: Contours of Skin friction coefficient over the rear slant combination of  $\sigma_{\omega_1}$  and  $\sigma_{\omega_2}$ ; sub figures (a) represents  $\sigma_{\omega_1} = 0.5$  and  $\sigma_{\omega_2} = 1.712$  and sub figures (b) represents  $\sigma_{\omega_1} = 0.65$  and  $\sigma_{\omega_2} = 1.712$

Due to the better prediction of the flow over the slant the flow prediction in the wake has also improved as seen from the Figure 5.11. The reattachment location in the wake has decreased from 236 mm to 208 mm which is closer to the experimental value of 190 mm and the prediction of the size of the separation bubble is better than the baseline case.

It was clear at this point that the variation of the closure coefficients in combination is giving a better flow prediction. So the present author further tried few combinations based on the results obtained from the individual parameters study. The closure coefficients  $\sigma_{\omega 1}$  and  $\sigma_{\omega 2}$  aids in predicting the  $C_d$  and  $C_l$  values close to the experiment and the choice of  $\beta^* = 0.07$  gave a better result in force and flow prediction than the default value. Based on the linear trends that the closure coefficients displayed, the present author came up with four sets of combinations as given in Table 5.7

Table 5.7: Variations of  $C_d$  and  $C_l$  for different combinations of  $\sigma_{\omega 1}$ ,  $\sigma_{\omega 2}$  and  $\beta^*$  compared against the experimental data of Strachan[8]

Case	$\sigma_{\omega 1}$	$\sigma_{\omega 2}$	$\beta^*$	$C_d$	$C_l$
$C_1$	0.35	1.1136	0.07	0.262	0.108
$C_2$	0.7	1.2	0.07	0.273	0.256
$C_3$	0.85	1.5	0.07	0.284	0.276
$C_4$	1	1.712	0.07	0.291	0.277
Experimental	-	-	-	0.300	0.280

From the Table 5.7, we can see that the case  $C_3$  has better agreement has the better agreement in  $C_d$  and  $C_l$  predictions with an underprediction of 2.6% and 1.07% respectively. We can see that the trends continue to exist as we increase  $\sigma_{\omega 1}$  and  $\sigma_{\omega 2}$ . The combination of  $\beta^* = 0.07$  gave a better correlation. From the Figure 5.12 we can see that case 4 performs better than the other cases as the reattachment location in the wake is better predicted in this case.

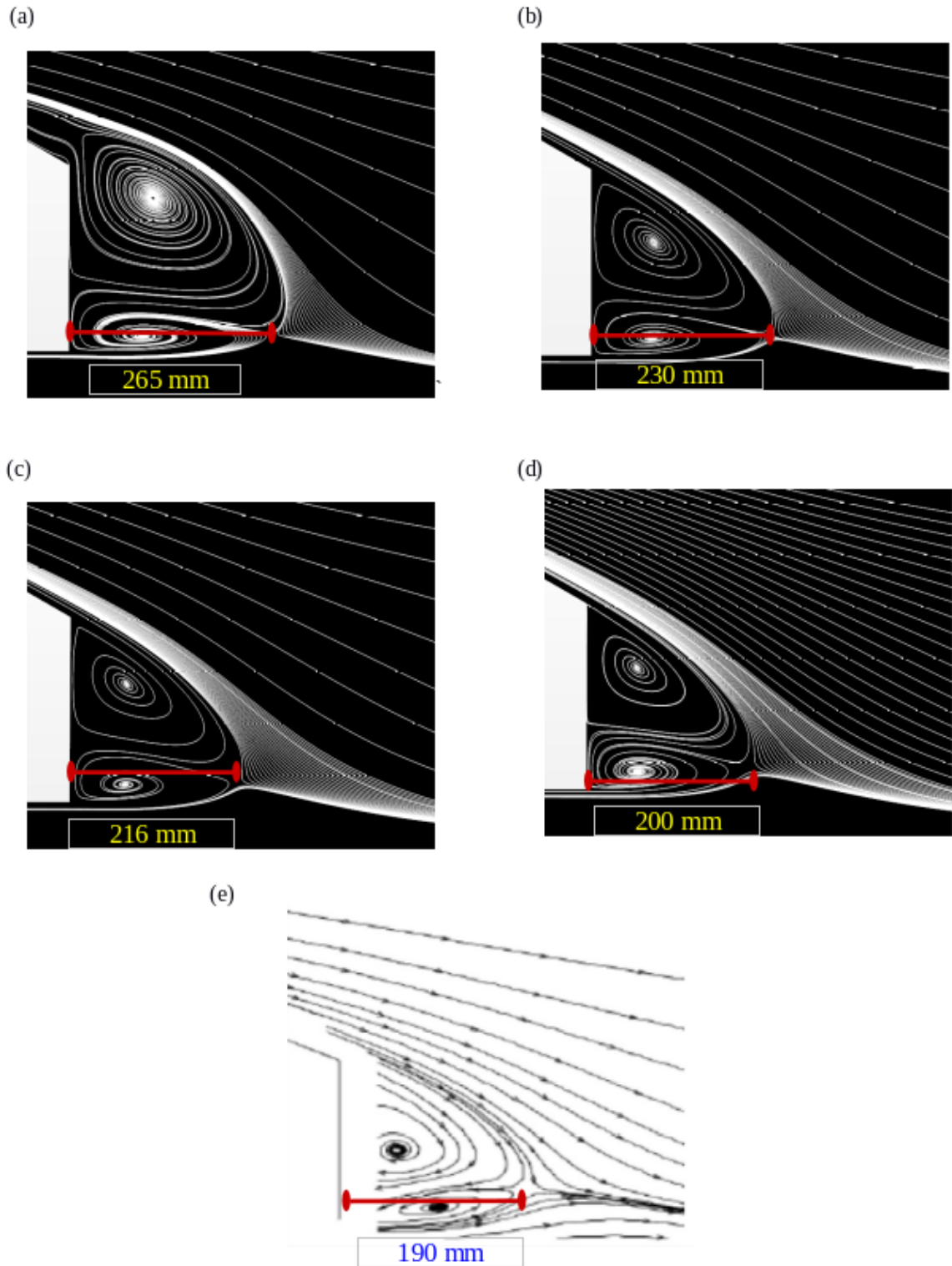


Figure 5.12: Contours of Streamlines for different combination of  $\sigma_{\omega 1}$  and  $\sigma_{\omega 2}$  and  $\beta^*$ ; sub figures (a) represents  $C_1$ , (b) represents  $C_2$ , (c) represents  $C_3$ , (d) represents  $C_4$ , (e) represents Experiments of Lienhart[5]

#### 5.4 Validation of the tuned set of closure coefficients

In this section, we will discuss in detail the performance of the best set of values for the closure coefficients for the flow predictions compared with experimental data of Strachan both qualitatively and quantitatively. In this validation study, Full body Mesh has been used along with the support sting as used in the original experiment of Strachan. Initially, RANS simulation is performed with the best set and later these coefficients are used in the IDDES formulation as it is a combination of RANS and LES. For the IDDES simulations default set of closure coefficients and a fine-tuned combination of turbulence closure coefficients are used for better flow predictions and the data is compared against the experimental data.

Table 5.8: Variations of  $C_d$  and  $C_l$  for With and without support sting.

	$C_d$	$C_l$
Current RANS-Without Sting	0.291	0.277
Current RANS-With Sting	0.293	0.264
Experiment[8]	0.300	0.280

From the Table 5.8 we can clearly discern that with inclusion of the strut there is an increase in the  $C_d$  value and prediction shifted more close to the experiment, but the  $C_l$  prediction has decreased, because of improper resolving of the support sting wake as it requires more finer mesh and is quite computationally expensive.

IDDES simulations have been formed for both Default and optimized set of closure coefficients and the data have been tabulated in the Table 5.9

Table 5.9: Variations of  $C_d$  and  $C_l$  for With and without support sting.

case	$C_d$	$C_l$
Default RANS	0.254	0.073
Default IDDES	0.332	0.312
Current RANS	0.293	0.264
Current IDDES	0.287	0.274
Experiment[8]	0.300	0.280

As we can observe from the Table 5.9 both modified RANS and modified IDDES performs better when compared to the default RANS and IDDES. Modified IDDES predicts  $C_d$  with an underprediction of 4.3% and  $C_l$  with 2.14 % when compared against the experimental values. The drag prediction of the Current IDDES with modified closure coefficients is less than the current RANS with modified closure coefficients is due to the underprediction of the surface drag over the body, but the Lift predictions are better as IDDES uses LES in the wake region. The force predictions are within 5% error, so the present author concludes that both modified RANS and IDDES are performing better, but modified IDDES has a slight edge over the RANS because of the level of resolving. We will investigate the flow fields for better comparison and analysis.

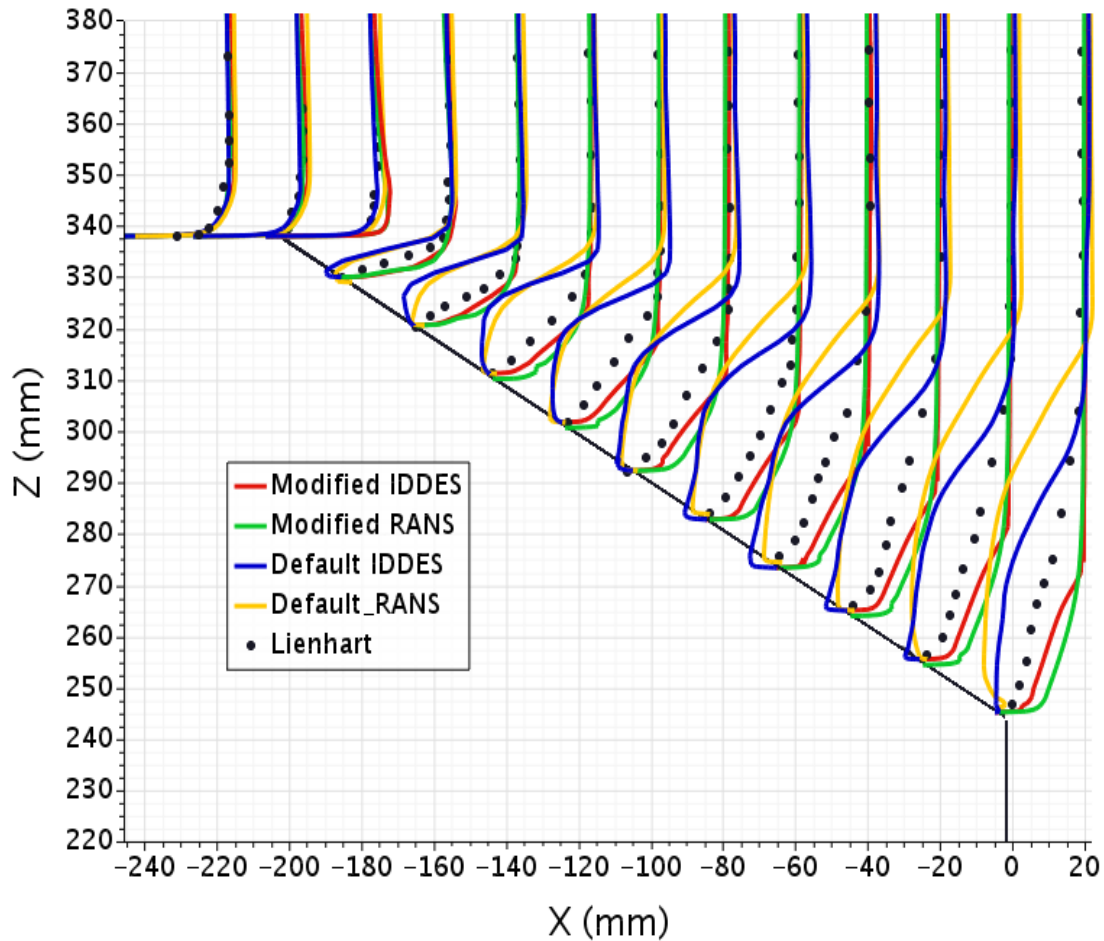


Figure 5.13: Streamwise velocity profiles over the rear slant for all the simulations represented in Table 5.9, compared against experimental data of Lienhart[5]

As the main drawback of the SST model is due to the underprediction of flow features near the rear slant region. We have investigated the velocity profiles on the rear slant taken at  $X/L = -0.233, -0.214, -0.194, -0.175, -0.156, -0.137, -0.118, -0.099, -0.08, -0.06, -0.041, -0.022, -0.003$  (where  $x/L = 0$  is at the rear of the body). These sections are in accordance with the experimental data of Lienhart[5]. At the locations  $x/L = -0.233, -0.214$  and  $-0.194$  i.e right before the slant, the flow predicted by all the models is identical. At the location  $x/L = -0.175$ , at the beginning of the slant region, both default RANS and IDDES underpredict the velocity recovery and the Modified IDDES and RANS predict close to the experiment. As the flow further

goes down the slant, default RANS and IDDES completely underpredicts the TKE over the slant and results in flow separation and fails to reattach. on the other hand, Modified RANS and IDDES slightly overpredict the velocity recovery over the slant. Modified IDDES slightly performs better than the Modified RANS model.

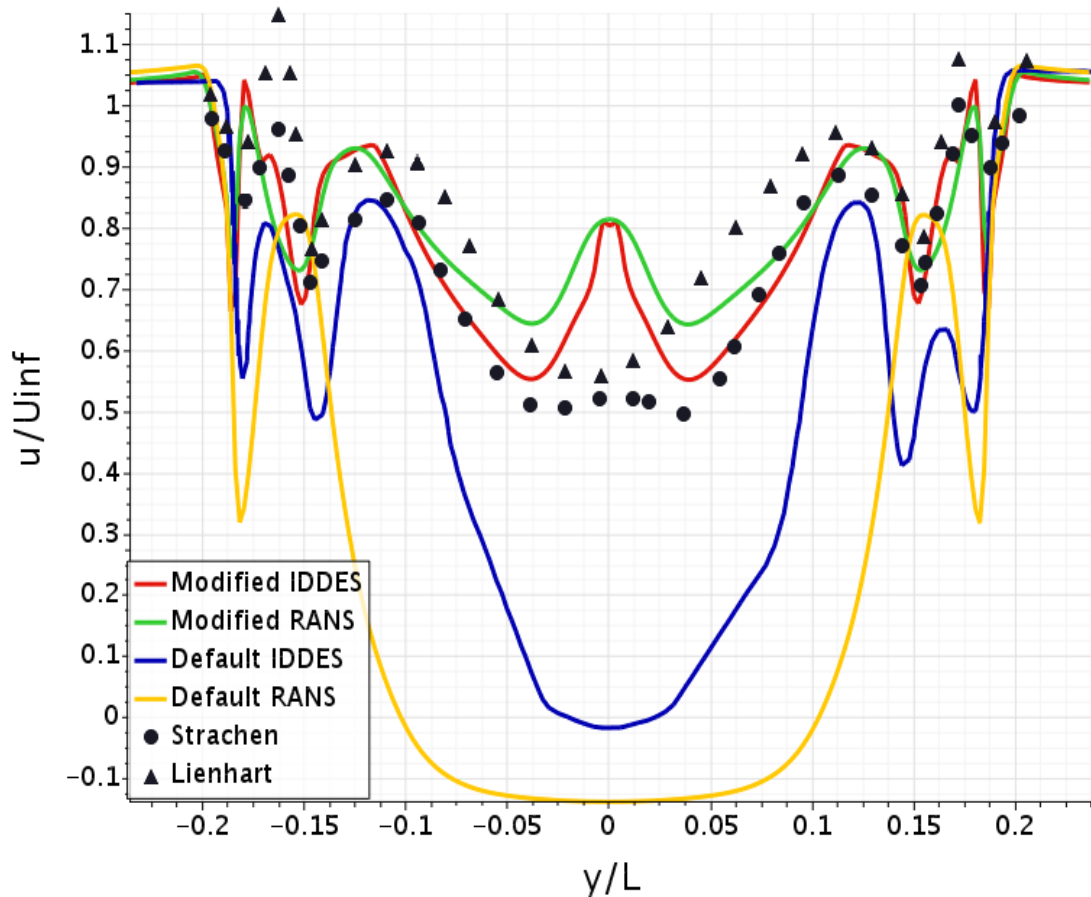


Figure 5.14: Transverse velocity profiles of normalized stream wise velocity over the trailing edge of the Ahmed body for all the simulations represented in Table 5.9, compared against experimental data of Strachan[8] and Lienhart[5]

The transverse velocity profiles of streamwise velocity component over the rear slant at the location  $x/L = 0$ , has been taken for all different models shown in 5.9 and the data have been plotted as shown in 5.14. Modified RANS and modified IDDES performs better when compared to Default RANS and IDDES. Both defaults IDDES and RANS predict separation over the slant. But modified RANS and IDDES

predict the separation and reattachment over the slant. The discrepancy in velocity prediction at the center line is attributed to the effect of the strut wake, as it requires finer mesh for resolving the support sting wake. A detailed comparison has been between the simulation with support sting and without sting as shown in Figure 5.15. Apart from this rest of the CFD predictions of Modified RANS and modified IDDES are in close agreement with the experimental values of Strachan and Lienhart.

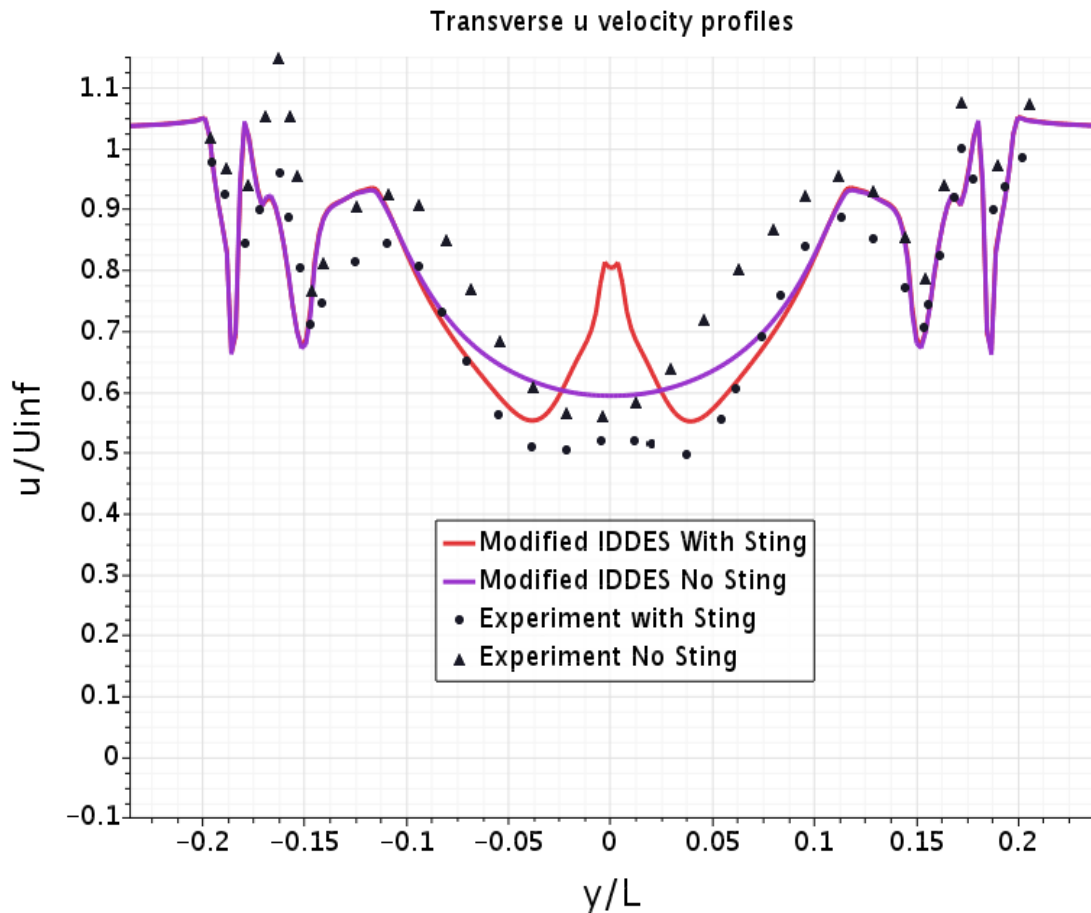


Figure 5.15: Transverse velocity profiles of normalized Stream wise velocity over the trailing edge of the Ahmed body for Current IDDES simulation with Sting and Current IDDES without Sting, compared against experimental data of Strachan[8] and Lienhart[5]

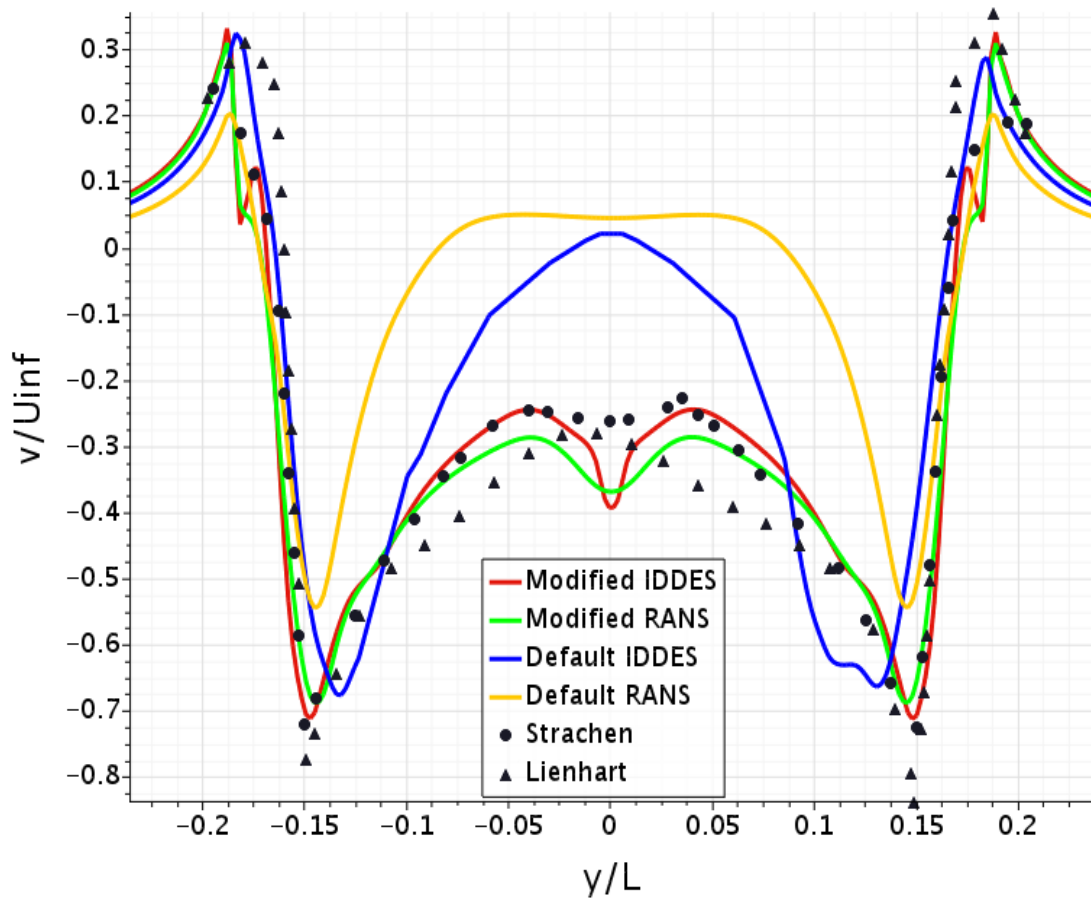


Figure 5.16: Transverse velocity profiles of normalized vertical velocity over the trailing edge of the Ahmed body for all the simulations represented in Table 5.9, compared against experimental data of Strachan[8] and Lienhart[5]

The transverse velocity profiles of vertical velocity component over the rear slant edge at the location  $y/L = 0.26$  is plotted as shown in 5.16. Initial inspection of the figure reveals that all the model predict the presence of longitudinal vortices. Default RANS underestimates the size and strength of these vortices, whereas default IDDES, predicts better than the default RANS models. Both Modified RANS and IDDES, predict close to the experimental data of Strachan and Lienhart. Modified IDDES captures the peaks better when compared to the Modified RANS. The dip in velocity at the centerline  $z/L = 0$  is due to the wake of the support sting, and this argument is supported by Figure 5.17, where we can clearly see that dip in velocity recovery

is slow because of the strut wake. similar trends are observed in the experiment of Strachan as he used support sting in his experiments and no dip in velocity is observed in Lienhart's experimental data as he used support struts at the bottom, instead of sting and the top.

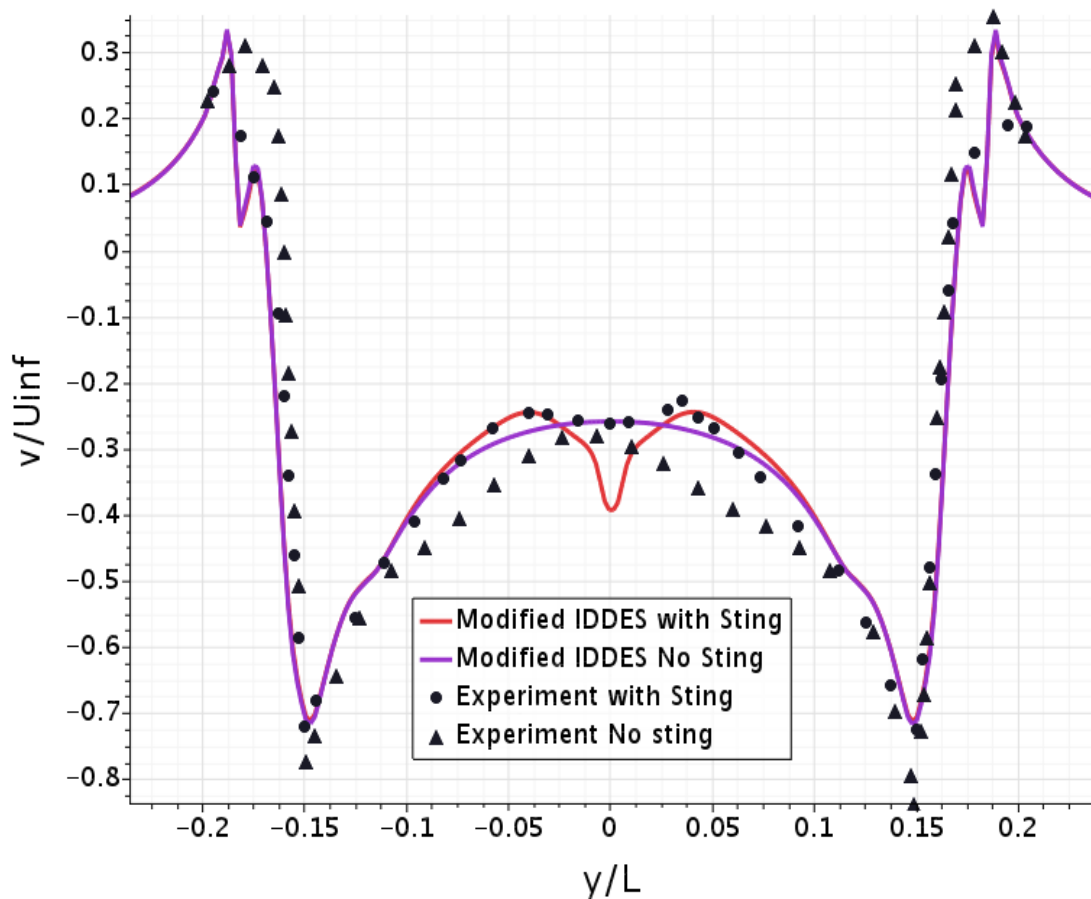


Figure 5.17: Transverse velocity profiles of normalized vertical velocity over the trailing edge of the Ahmed body for Current IDDES simulation with Sting and Current IDDES without Sting, compared against experimental data of Strachan[8] and Lienhart[5]

Velocity profiles in wake are studied at the location  $y/L = 0.15$  and  $x/L = 0.5$ . The stream wise velocity component and the vertical components are compared. From the Figure 5.18 we can see the drops in the streamwise velocity due to the total pressure loss caused by the longitudinal vortices. Default RANS overpredicts the velocity

drop because of the weaker longitudinal vortices and Current RANS underpredicts the strength of the vortices. Default IDDES predicts the strength of the longitudinal vortices but fails to predict the velocity recovery in the center plane due to the separation flow predicted over the rear slant. Modified IDDES captures the Strength and predicts the velocity recovery closer to the experiments of Lienhart. Again the dip in the velocity is due to the wake of the Sting.

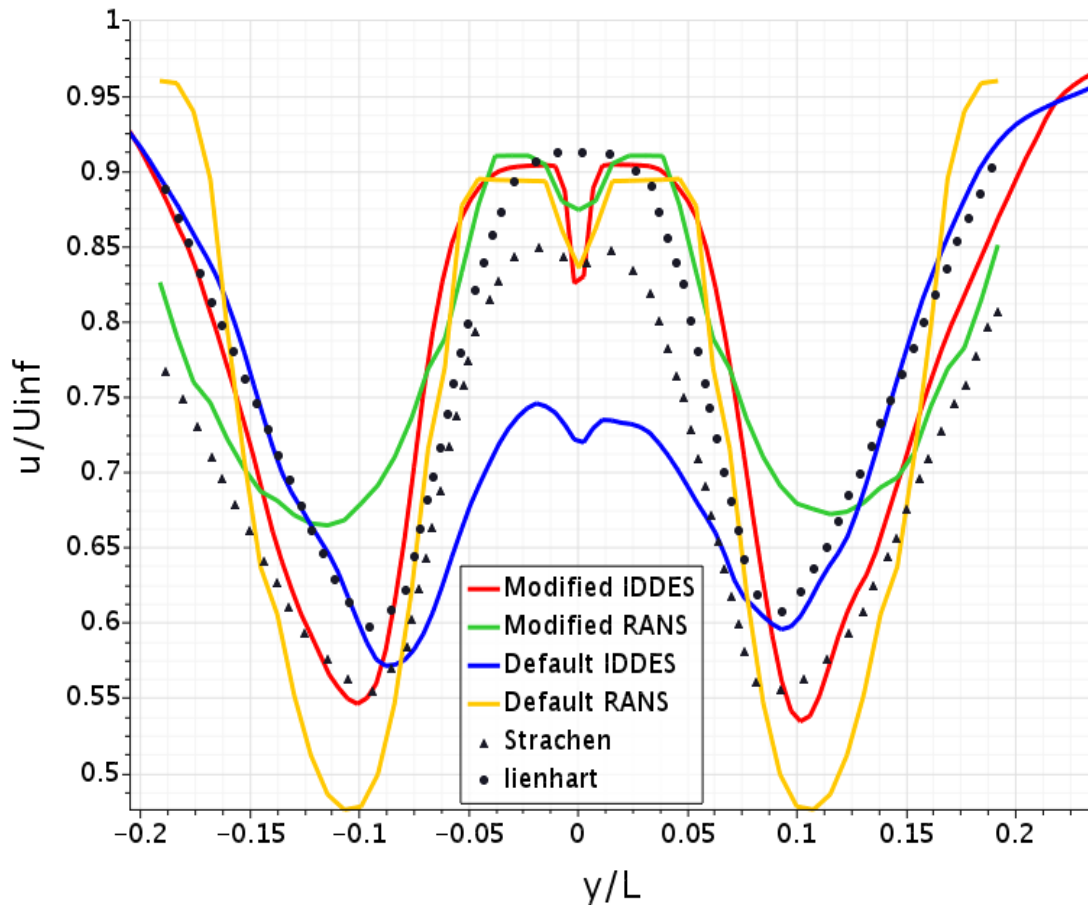


Figure 5.18: Transverse velocity profiles of normalized stream wise velocity at location  $x/L = 0.5$  and  $y/L = 0.15$  for all the simulations represented in 5.9, compared against experimental data of Strachen[8] and Lienhart[5]

From the Figure 5.19, we can see the vertical velocity profiles for all the simulations at the location  $y/L = 0.15$  and  $x/L = 0.5$ . We can clearly see the downwash produced the backlight can be seen. As the flow continues downstream, the vortex centers

continue to move towards the model centerline ( $z/L=0$ ). All models under-predict the strength of the vortex cores except for the Current IDDES which predicts in close agreement with the experiments of Lienhart[5].

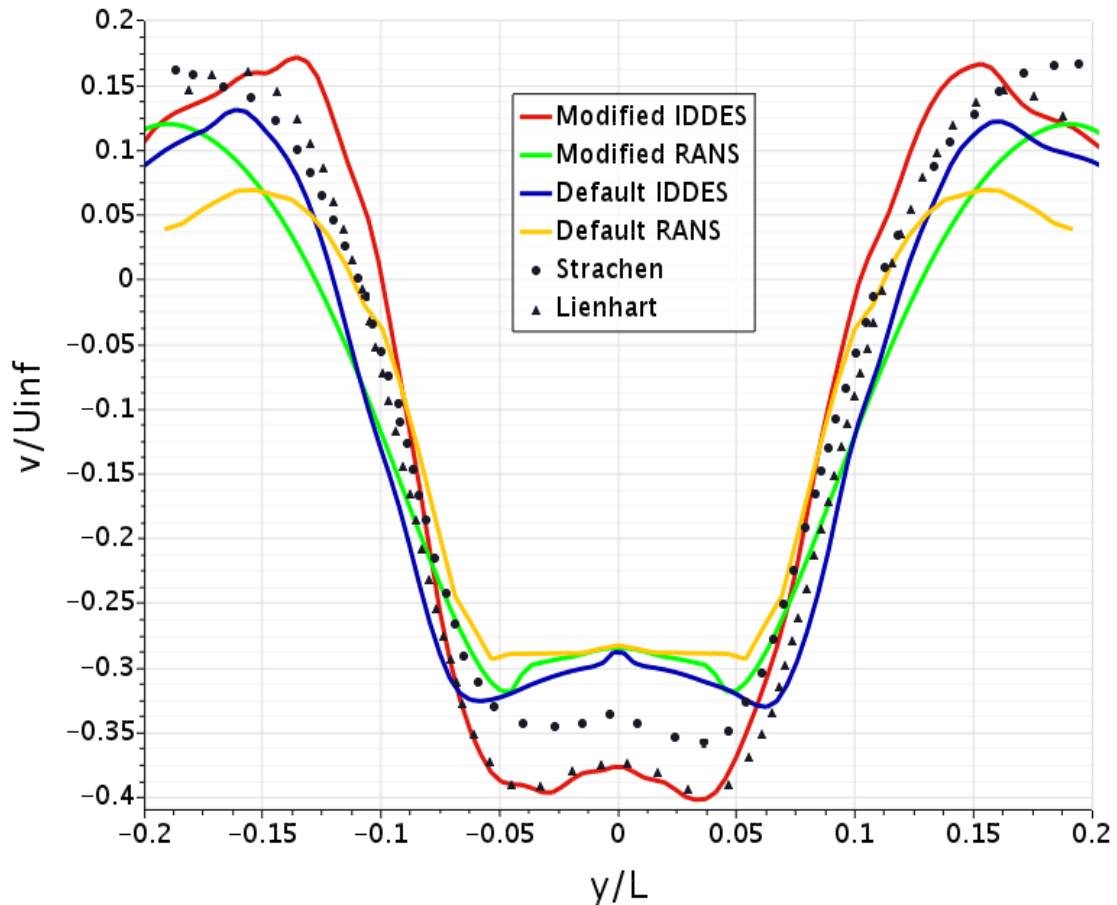


Figure 5.19: Transverse velocity profiles of normalized vertical velocity at location  $x/L = 0.5$  and  $y/L = 0.15$  for all the simulations represented in 5.9, compared against experimental data of Strachan[8] and Lienhart[5]

We will now compare contour plots of Streamwise velocities for all the simulations. As seen from the Figure 5.20 the contour plots of  $u$  velocity at  $0.077L$  downstream of the model. We can clearly see the formation of the longitudinal vortices for all the models but the current IDDES model has a close agreement with the experiment of Strachan. At the model centerline, we can clearly see the influence of sting wake on the flow predictions.

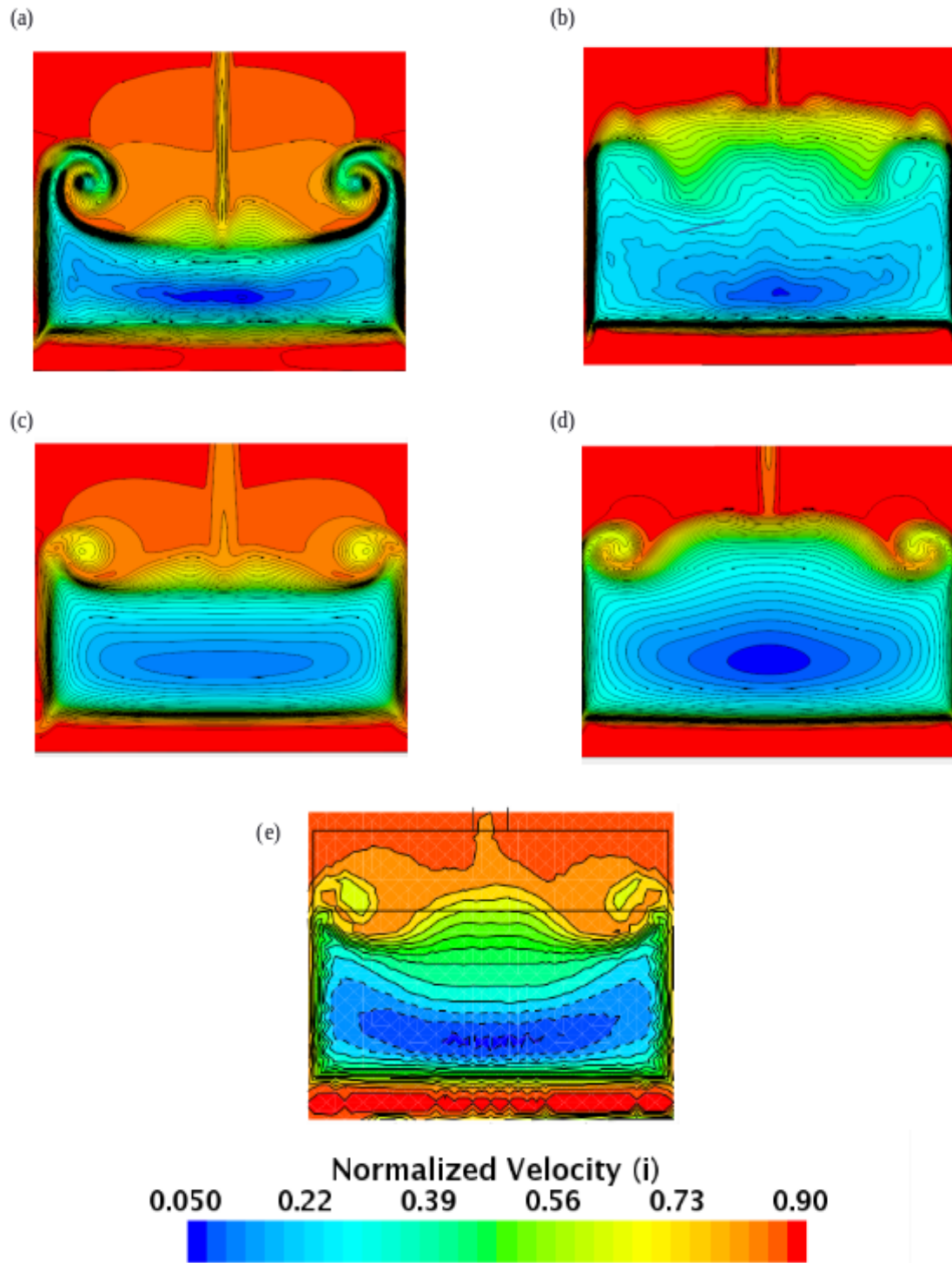


Figure 5.20: Contour plots of normalized streamwise velocity at location  $x/L = 0.077$ ; sub figures (a) Modified IDDES, (b) Default IDDES, (c) Modified RANS, (d) Default RANS, (e) Experiment[8]

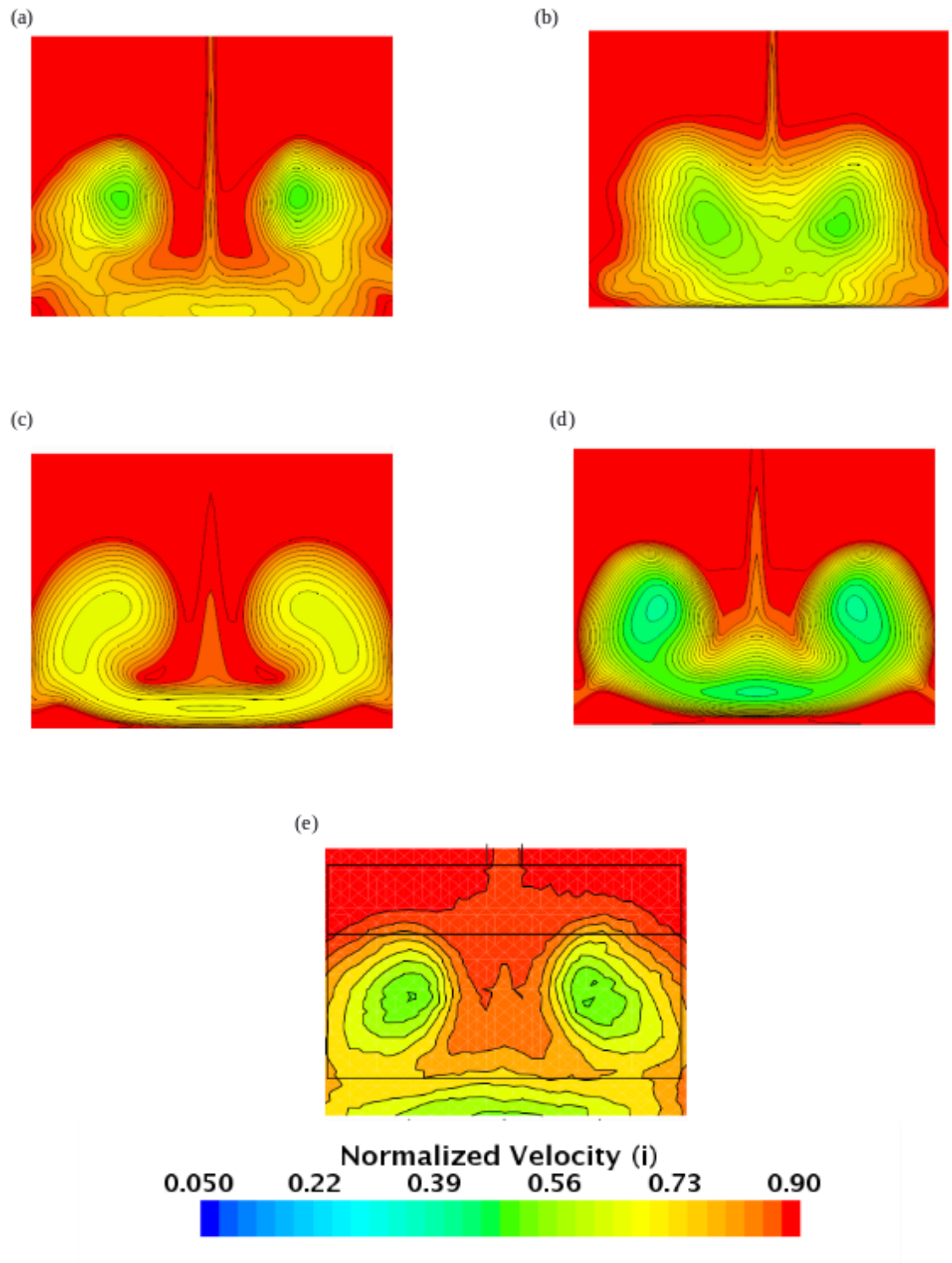


Figure 5.21: Contour plots of normalized streamwise velocity at location  $x/L = 0.5$ ; sub figures (a) Modified IDDES, (b) Default IDDES, (c) Modified RANS, (d) Default RANS, (e) Experiment[8]

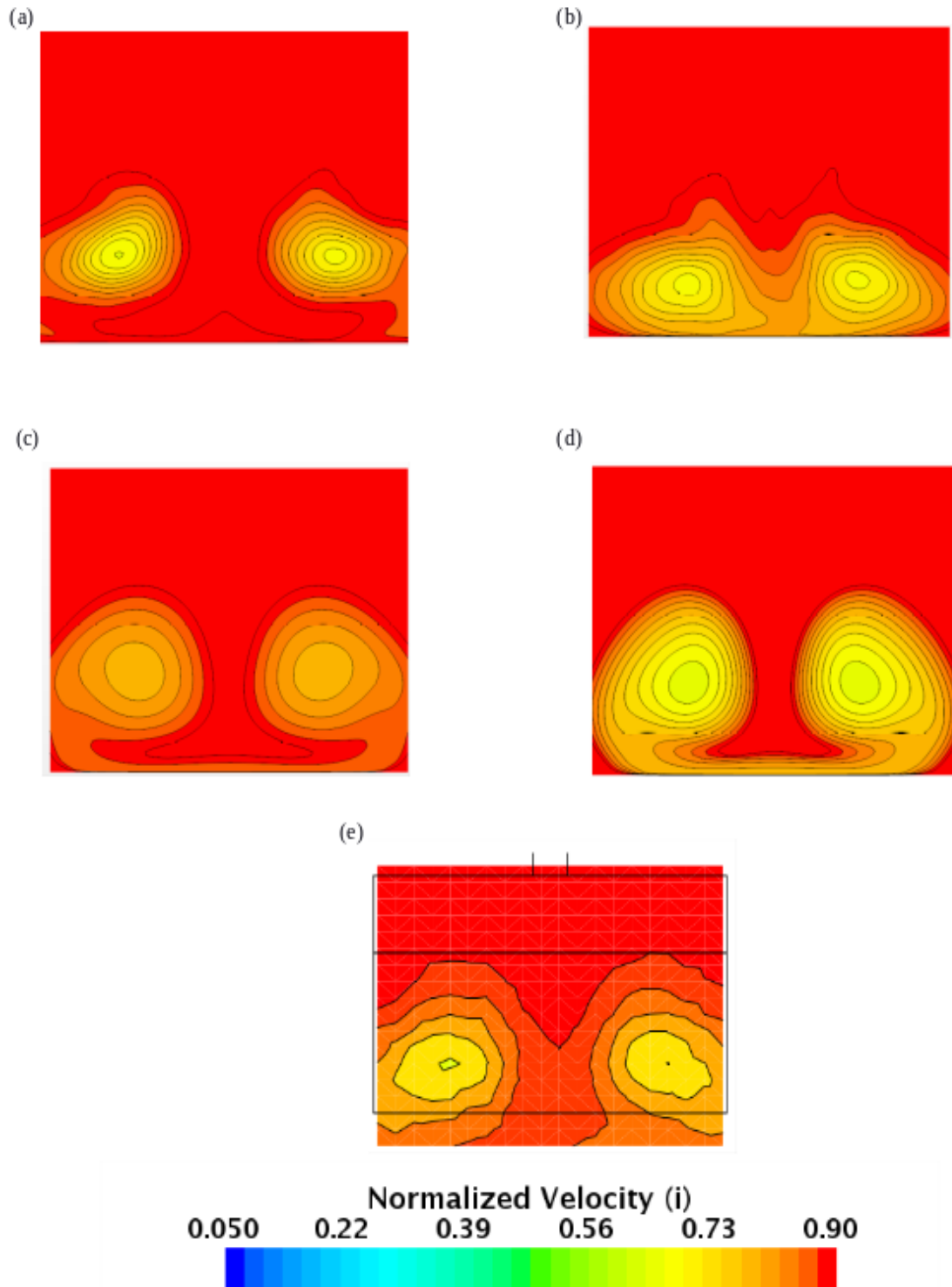


Figure 5.22: Contour plots of normalized streamwise velocity at location  $x/L = 1$ ; sub figures (a) Modified IDDES, (b) Default IDDES, (c) Modified RANS, (d) Default RANS, (e) Experiment[8]

Figures 5.21 and 5.22 represents the contour plots of  $u$  velocity at  $x/L=0.5$  and  $x/L=1$  respectively. Inspection of these contour plots shows the expansion of the vortices further in the wake. We can see a small region of backward flow due to the effect of the supporting sting at location  $x/L=0.5$ , but at the location  $x/L=1$ , this effect is not seen. For the present simulations, this effect is stronger than the experimental due to the improper resolving of the wake. Among all the models Current IDDES predicts flow close to the experiment as it uses LES away from the walls and LES has a higher resolution when compared to the RANS.

The contour plots of Pressure coefficient have been plotted as shown in 5.23 for all the models and compared against the experimental data of Starchan[8] and Lienhart[5]. The regions of lower  $c_p$  at the slant edges show the existence of the side vortices. Higher velocity flow forms the lower pressure over the slant region. Default IDDES and Default RANS underpredict the strength of the counter-rotating vortices. Current IDDES and Current RANS has better  $C_p$  prediction and is in close agreement with the experiments, except in the slant beginning as the Current models predict surface pressure lower than that recorded in the experiments.

From the Figure 5.24 we can see the reattachment locations of all the models compared to the experiment of Lienhart. The Default RANS overpredicts the reattachment region in the wake region. Current RANS and IDDES predict the reattachment location closer to the experiment, but the RANS model predicts the location of the saddle points one below the other, but the current IDDES predicts the saddle points close to the experiment.

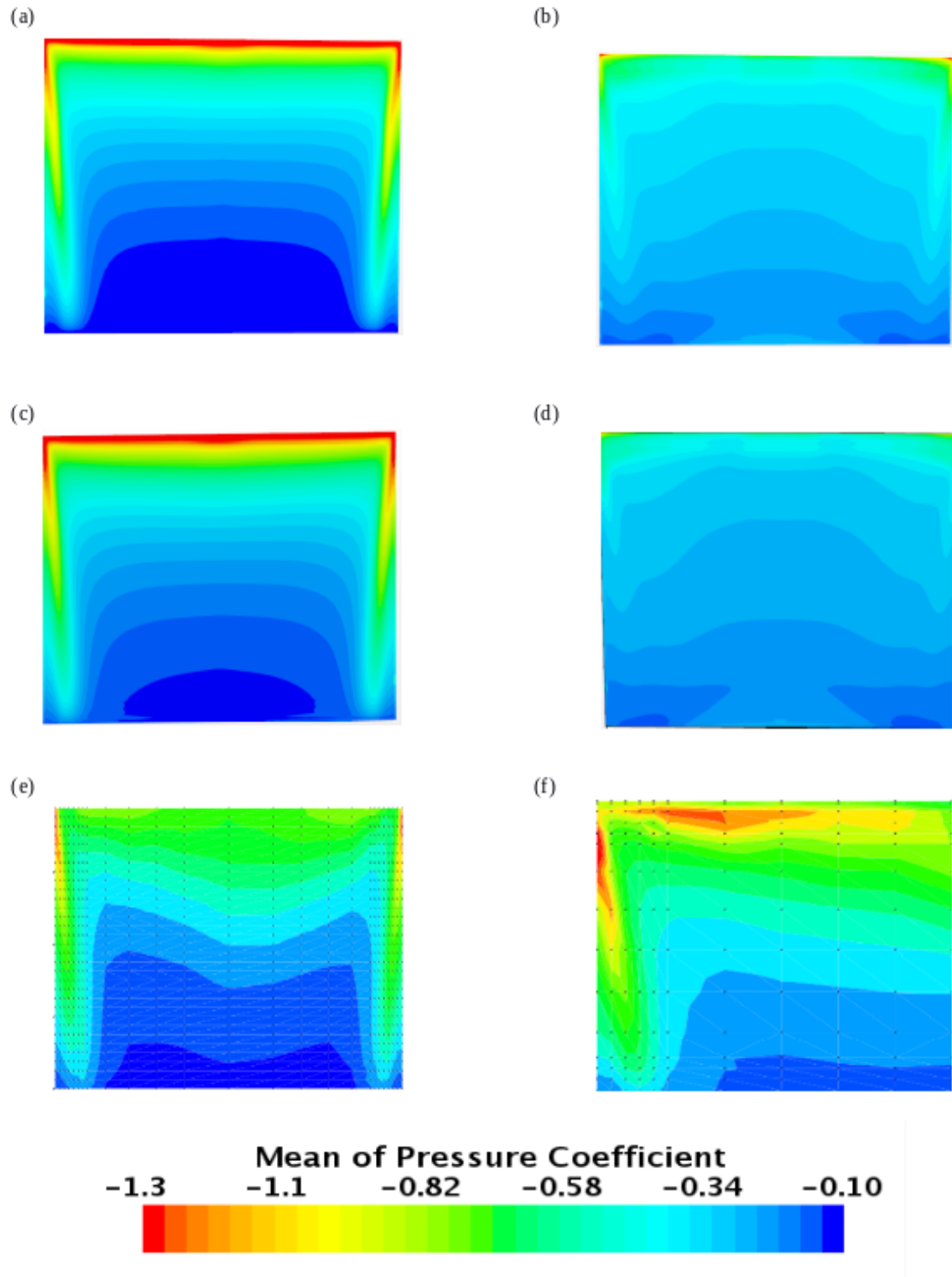


Figure 5.23: Contour plots of coefficient of pressure distribution ; sub figures (a) Modified IDDES,(b) Default IDDES, (c) Modified RANS, (d) Default RANS, (e) Experiment[8]

, (f) Experiment[5]

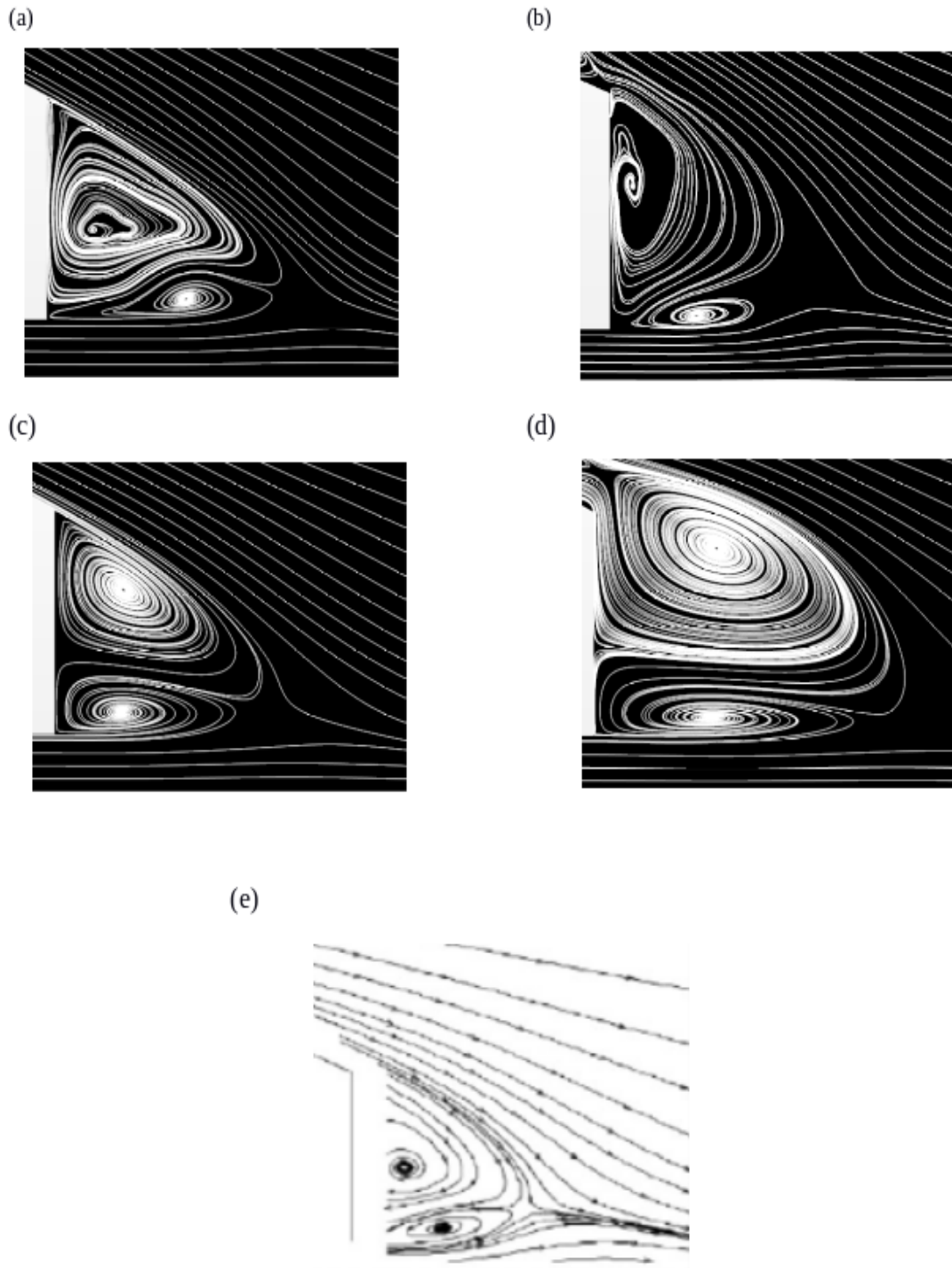
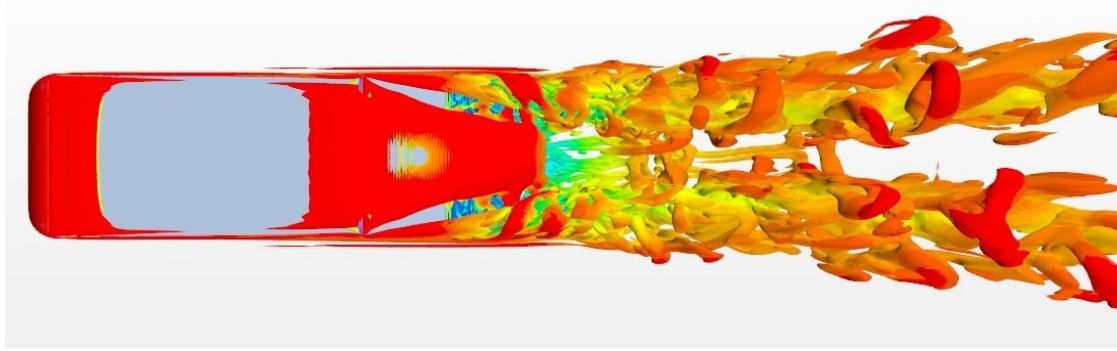
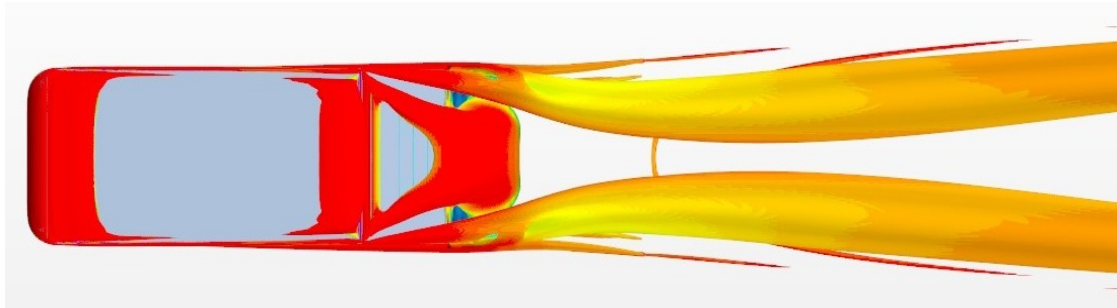


Figure 5.24: Streamlines in the wake of Ahmed body; sub figures (a) Modified IDDES, (b) Default IDDES, (c) Modified RANS, (d) Default RANS, (e) Experiment[8]



(a) Current IDDES



(b) Current RANS

Figure 5.25: Iso surfaces of Normalized Q-criterion = 60.

The above Figure 5.25 clearly illustrates the complex flow associated with the current geometry. We can clearly observe the spanwise trailing wake and the streamwise C-pillar vortices. These C-pillar vortices are extended far downstream and affect the trailing wake structure through a complex three-dimensional interaction. The above figure also illustrates the difference in the level of resolving turbulence in the wake.

### 5.5 Implementation of closure coefficients modification for other rear slant angles

In this section, we will continue this study to Ahmed body with other rear slant angles and examine the effect of tuning the closure coefficients on the flow predictions. Ahmed body with a rear slant angle of  $20^\circ$  and  $35^\circ$  have been used, with the availability of the experimental data. The baseline case for the above-mentioned slant angles have been performed and then later the closure coefficients are tuned based on the work done and results obtained from the previous sections.

Table 5.10: Variations of  $C_d$  and  $C_l$  for Ahmed body with rear slant angle  $\phi=20^\circ$ .

case	$C_d$	$C_l$
Baseline	0.226	0.177
Optimized set for $25^\circ$	0.280	0.220
Optimized set for $20^\circ$	0.238	0.189
Experiment[25]	0.245	0.190

The force predictions of the baseline case are compared with the experiment of strachan[25] and we can see that the  $C_d$  and  $C_l$  are underpredicted by 7.7% and 6.3% respectively. Initially, the best set obtained for the validation study i.e Ahmed body with a rear slant angle of  $\phi=25$  deg has been used and the results are recorded as seen in 5.10. We can clearly see that the  $C_d$  and  $C_l$  are overpredicted 14.2% and 15.7% respectively. This trend is expected as slant angle is different for both the cases and from the literature we know that rear slant angle plays a huge role in the flow predictions. So the set of closure coefficients worked for rear slant angle  $\phi=25$  degrees will not work for rear slant angle  $\phi=20^\circ$ .

This gave the present author an clear idea that the tuning of the closure coefficients depends on the geometry and they are not constant. Now the used the knowledge gained from the rigorous study of the 25 degree slant angle and repeated similar study as mentioned in the previous sections for the Current set [ $\sigma_{\omega_1}=0.6$ ,  $\sigma_{\omega_2}=1.1136$ ,  $\beta^*=0.07$ ] has obtained better results with almost spot on value of the lift prediction and the drag under prediction has reduced from 7.7% to 2.8%.

To further strengthen the argument the results from rear slant angle  $\phi=35$  have been analyzed.

Table 5.11: Variations of  $C_d$  and  $C_l$  for Ahmed body with rear slant angle  $\phi=35^\circ$ .

Case	$C_d$	$C_l$
Baseline	0.238	-0.078
Optimized set for $25^\circ$	0.350	0.120
Optimized set for $35^\circ$	0.279	-0.018
Experiment[25]	0.279	-0.047
Experiment[26]	0.279	0.004
Guilmineau(CFD)[27]	0.315	-0.015

This work on rear slant angle( $\phi = 35^\circ$ ) further strengthens the argument that the tuning of the closure coefficients can be applied for other geometries and the level of tuning depends on the geometry, but the influence of the tuning coefficients are almost similar. As seen from the Table 5.11 Current set [ $\sigma_{\omega_1}=0.7$ ,  $\sigma_{\omega_2}=1.2$ ,  $\beta^* =0.07$ ] has the  $C_d$  prediction spot on with the experiments of Strachan[25] and Meile et al.[26]. There is a noticeable difference on the  $C_l$  prediction, but the author speculates that the difference in  $C_l$  between the two experiments is intriguing and DES work of Guilmineau did not predict the downforce as high as Strachan. From this, the present author highly doubts the credibility of the lift data provided for the 35 deg rear slant angle.

Table 5.12: Best results for Ahmed body with all rear slant angles compared against experiment of Strachan[25].

Slant angle	$\sigma_{\omega_1}$	$\sigma_{\omega_2}$	$\beta^*$	$C_d$		$C_l$	
				Optimized	Experiment	Optimized	Experiment
$20^\circ$	0.6	1.1	0.07	0.238	0.245	0.189	0.190
$25^\circ$	1.0	1.712	0.07	0.291	0.300	0.277	0.280
$35^\circ$	0.7	1.2	0.07	0.279	0.279	-0.047	-0.018

## CHAPTER 6: CONCLUSIONS

A successful investigation on the performance and sensitivity of the turbulence model closure coefficients of SST  $k - \omega$  turbulence model in predicting flow past a simplified road vehicle was completed and the best set of closure coefficients have been formulated that gave well-correlated results with the experiments. The original SST model given by Mentor[23] even with sufficient near-wall resolution ( $y^+ < 1$ ) and with mesh independence, was unable to predict the correct level of Turbulent Kinetic Energy (TKE) in the initial separated shear layer. Due to this underprediction of TKE, the separation bubble over the rear slant is overpredicted.

The current study showed that the calibration of SST  $k - \omega$  turbulence model closure coefficients based on observed turbulence properties of the simple canonical flows, inadequately resolve separated flows. A detailed investigation of the influence of closure coefficients  $\sigma_{\omega 1}$ ,  $\sigma_{\omega 2}$ ,  $\beta^*$ , on the flow prediction was carried out, while, in anticipation of their negligible contributions, analyses on the sensitivities of the  $k$ -equation closure coefficients,  $\sigma_{k1}$  and  $\sigma_{k2}$ , were ignored based of some initial investigations. Individual analysis of these closure coefficients on the force and flow predictions showed that  $\sigma_{\omega 2}$  had most discernible influence on the predictions. A linear trend was observed for the force predictions for  $\sigma_{\omega 1}$  and  $\sigma_{\omega 2}$ . On the other hand  $\beta^*$  had a significant effect on the flow predictions but a linear trend was not observed.

Even though the tuning of individual parameter had a significant effect, but this was not enough to predict the exact flow features. Then the combination of these closure coefficients has been tested. For  $\sigma_{\omega 1} = 1.0$ ,  $\sigma_{\omega 2} = 1.712$  and  $\beta^* = 0.07$ , the  $C_d$  and  $C_l$  predictions were better than the original SST model and closer to the experimental value.

The above-reported values for the closure coefficients were further applied to the IDDES simulation with sufficient grid resolution. IDDES simulation improved the prediction of flow field when compared to the RANS, but slightly underpredicted  $C_d$  and over predicted  $C_l$ . In order to validate the results obtained from the simulations, the data was compared with the experiments of Strachan[8]. For the exact comparison with experiment, an overhead support sting was included. The current mesh was not sufficient enough to resolve the wake of the strut, which resulted in a slight difference in the force and flow predictions. The force predictions from the CFD correlated well with the experiment[8], along with a good agreement with the flow fields.

The tuning of the closure coefficients is case dependent and their values cannot be universal. This argument was further supported by applying the tuning of closure coefficients for the flow predictions over Ahmed body with different rear slant angles ( $\phi=20^\circ$  and  $35^\circ$ ). The best combination of closure coefficients obtained from the previous study with 25 degrees was implemented for these cases. Clearly, there was a huge overprediction of force coefficients. This is clearly attributed to the complex flow nature of the 25 deg rear slant angle when compared to  $20^\circ$  and  $35^\circ$  rear slant angles where the flow is either attached or separated. The linear trends observed in the  $25^\circ$  rear slant angle was used and lower values of closure coefficients have been used for other slant angles and few cases were performed and the results obtained had good agreement with the experimental values.

The main takeaway from this thesis is that the investigation carried can be considered as a decent approach, as the results obtained after tuning the closure coefficients are consistent with the multitudes of experimental data available and also had good agreement with the flow fields. These results are quite promising for improving the force predictions using SST  $k - \omega$  model for automotive flows. The equilibrium assumption used in postulating the turbulence model transport equations is no longer valid for the non-equilibrium flows. The closure coefficients will no longer be constants

but will be variables depending on the flow parameters.

### 6.1 Future Research

While there is an extraordinary level of research associated with the generic car models, this research marks a new pathway for obtaining well correlated results. The formulation of closure coefficients for the non equilibrium flows further requires DNS or LES investigations.

## REFERENCES

- [1] S. R. Ahmed, G. Ramm, and G. Falin, "Some salient features of the time-averaged ground vehicle wake," *SAE Transactions*, pp. 473–503, 1984.
- [2] E. Guilmineau, "Numerical simulations of flow around a realistic generic car model," *SAE International Journal of Passenger Cars-Mechanical Systems*, vol. 7, no. 2014-01-0607, pp. 646–653, 2014.
- [3] A. I. Heft, T. Indinger, and N. A. Adams, "Introduction of a new realistic generic car model for aerodynamic investigations," tech. rep., SAE Technical Paper, 2012.
- [4] B. Zhang, S. To, and Y. Zhou, "Strouhal numbers of unsteady flow structures around a simplified car model," in *Fluid-Structure-Sound Interactions and Control*, pp. 179–184, Springer, 2014.
- [5] H. Lienhart and S. Becker, "Flow and turbulence structure in the wake of a simplified car model," tech. rep., SAE Technical Paper, 2003.
- [6] I. Bayraktar, D. Landman, and O. Baysal, "Experimental and computational investigation of ahmed body for ground vehicle aerodynamics," tech. rep., SAE Technical Paper, 2001.
- [7] T. Tunay, B. Sahin, and V. Ozbolat, "Effects of rear slant angles on the flow characteristics of ahmed body," *Experimental Thermal and Fluid Science*, vol. 57, pp. 165–176, 2014.
- [8] R. Strachan, K. Knowles, and N. Lawson, "The vortex structure behind an ahmed reference model in the presence of a moving ground plane," *Experiments in fluids*, vol. 42, no. 5, pp. 659–669, 2007.
- [9] S. KrajnoviÄ and L. Davidson, "Flow around a simplified car, part 1: large eddy simulation," *Journal of Fluids Engineering*, vol. 127, no. 5, pp. 907–918, 2005.
- [10] C. Hinterberger, M. Garcia-Villalba, and W. Rodi, "Large eddy simulation of flow around the ahmed body," in *The aerodynamics of heavy vehicles: trucks, buses, and trains*, pp. 77–87, Springer, 2004.
- [11] E. SERRE, M. MINGUEZ, R. PASQUETTI, E. GUILMINEAU, and G. B. DENG, "Turbulent flow around the ahmed body: a french-german collaborative evaluation of les," 2011.
- [12] E. Guilmineau, "Computational study of flow around a simplified car body," *Journal of wind engineering and industrial aerodynamics*, vol. 96, no. 6-7, pp. 1207–1217, 2008.

- [13] N. Ashton, A. Revell, and R. Poletto, “Grey-area mitigation for the ahmed car body using embedded ddes,” in *Progress in Hybrid RANS-LES Modelling*, pp. 119–129, Springer, 2015.
- [14] R. Maduta and S. Jakirlic, “Improved rans computations of flow over the 25°-slant-angle ahmed body,” *SAE International Journal of Passenger Cars-Mechanical Systems*, vol. 10, no. 2017-01-1523, pp. 649–661, 2017.
- [15] H. Tennekes, J. L. Lumley, J. Lumley, *et al.*, *A first course in turbulence*. MIT press, 1972.
- [16] L. Davidson, *An introduction to turbulence models*. 1997.
- [17] R. Cant, “Sb pope, turbulent flows, cambridge university press, cambridge, uk,” *Combustion and Flame*, vol. 125, pp. 1361–1362, 2001.
- [18] C. Argyropoulos and N. Markatos, “Recent advances on the numerical modelling of turbulent flows,” *Applied Mathematical Modelling*, vol. 39, no. 2, pp. 693–732, 2015.
- [19] D. C. Wilcox *et al.*, *Turbulence modeling for CFD*, vol. 2. DCW industries La Canada, CA, 1998.
- [20] B. Launder and D. Spalding, “The numerical computation of turbulent flows. computer methods in applied mechanics and energy, 3, 269–289,” 1974.
- [21] D. C. Wilcox, “Reassessment of the scale-determining equation for advanced turbulence models,” *AIAA journal*, vol. 26, no. 11, pp. 1299–1310, 1988.
- [22] F. Menter, “Zonal two equation kw turbulence models for aerodynamic flows,” in *23rd fluid dynamics, plasmadynamics, and lasers conference*, p. 2906, 1993.
- [23] F. R. Menter, “Two-equation eddy-viscosity turbulence models for engineering applications,” *AIAA journal*, vol. 32, no. 8, pp. 1598–1605, 1994.
- [24] M. L. Shur, P. R. Spalart, M. K. Strelets, and A. K. Travin, “A hybrid rans-les approach with delayed-des and wall-modelled les capabilities,” *International Journal of Heat and Fluid Flow*, vol. 29, no. 6, pp. 1638–1649, 2008.
- [25] R. K. Strachan, “The aerodynamic interference effects of side wall proximity on a generic car model,” 2010.
- [26] W. Meile, G. Brenn, A. Reppenhagen, and A. Fuchs, “Experiments and numerical simulations on the aerodynamics of the ahmed body,” *CFD letters*, vol. 3, no. 1, pp. 32–39, 2011.
- [27] E. Guilmineau, G. Deng, A. Leroyer, P. Queutey, M. Visonneau, and J. Wackers, “Assessment of hybrid rans-les formulations for flow simulation around the ahmed body,” *Computers & Fluids*, 2017.